
A Machine Learning–Enhanced Hopf–Cole Formulation for Nonlinear Gas Flow in Porous Media

AN E-PRINT OF THIS PAPER IS AVAILABLE ON ARXIV.

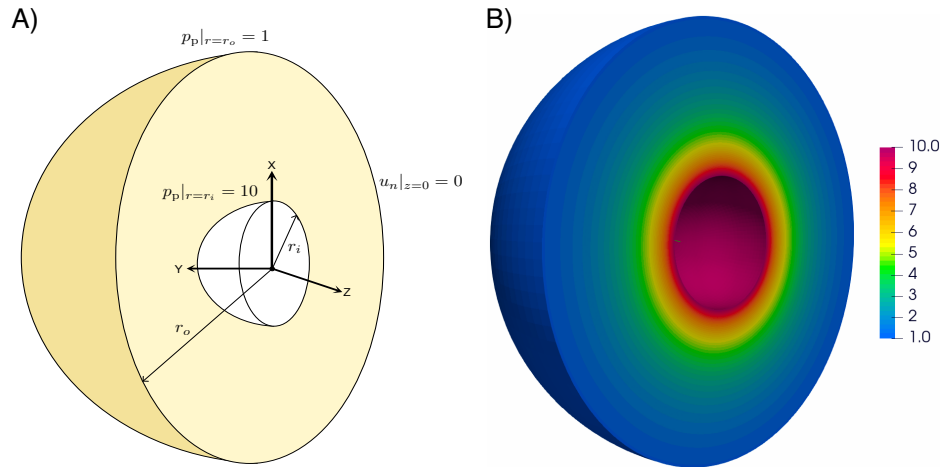
AUTHORED BY

VENKAT S. MADURI

*Graduate Student, Department of Civil & Environmental Engineering
University of Houston, Houston, Texas 77204.*

K. B. NAKSHATRALA

*Department of Civil & Environmental Engineering
University of Houston, Houston, Texas 77204.
phone: +1-713-743-4418, e-mail: knakshatrala@uh.edu
website: <http://www.cive.uh.edu/faculty/nakshatrala>*



A) This figure illustrates the three-dimensional concentric spherical porous domain with inner radius r_i and outer radius r_o with prescribed pressure on the spherical boundaries $p_p|_{r=r_i} = 10$ and $p_p|_{r=r_o} = 1$ together with a symmetry condition on the cut plane $z = 0$ enforcing zero normal flow. B) Shows the resulting pressure profile across the domain demonstrating that the proposed framework delivers stable high-fidelity predictions.

A Machine Learning–Enhanced Hopf–Cole Formulation for Nonlinear Gas Flow in Porous Media

Venkat S. Maduri and Kalyana B. Nakshatrala

Department of Civil and Environmental Engineering

University of Houston, Houston, Texas 77204, USA.

Correspondence to: knakshatrala@uh.edu, +1-713-743-4418

ABSTRACT. Accurate modeling of gas flow through porous media is critical for many technological applications, including reservoir performance prediction, carbon capture and sequestration, and fuel cells and batteries. However, such modeling remains challenging due to strong nonlinear behavior and uncertainty in model parameters. In particular, gas slippage effects described by the Klinkenberg model introduce pressure-dependent permeability, which complicates numerical simulation and obscures deviations from classical Darcy flow behavior. To address these challenges, we present an integrated modeling framework for gas transport in porous media that combines a Klinkenberg-enhanced constitutive relation, Hopf–Cole–transformed mixed-form linear governing equations, a shared-trunk neural network architecture, and a Deep Least-Squares (DeepLS) solver. The Hopf–Cole transformation reformulates the original nonlinear flow equations into an equivalent linear system closely related to the Darcy model, while the mixed formulation, together with a shared-trunk neural architecture, enables simultaneous and accurate prediction of both pressure and velocity fields. A rigorous convergence analysis is performed both theoretically and numerically, establishing the stability and convergence properties of the proposed solver. Importantly, the proposed framework also naturally facilitates inverse modeling of pressure-dependent permeability and slippage parameters from limited or indirect observations, enabling efficient estimation of flow properties that are difficult to measure experimentally. Numerical results demonstrate accurate recovery of flow dynamics and parameters across a wide range of pressure regimes, highlighting the framework’s robustness, accuracy, and computational efficiency for gas transport modeling and inversion in tight formations.

Acronyms and Abbreviations

| | |
|--------|----------------------------------|
| DeepLS | Deep Least-Squares |
| DRM | Deep Ritz Method |
| FEM | Finite Element Method |
| PDE | Partial Differential Equation |
| PINNs | Physics-Informed Neural Networks |

Key words and phrases. deep least-squares method; Klinkenberg effect; Hopf–Cole transformation; inverse modeling; nonlinear gas flow through porous media; convergence analysis.

1. INTRODUCTION AND MOTIVATION

THE flow of gas through porous media is fundamental to a wide range of industrial and environmental processes [Bear, 2013]. Key examples include:

- (1) **Energy sector:** Gas transport controls production in both conventional and unconventional reservoirs, including tight sands and shale formations, where accurate modeling is essential for efficient resource recovery [Florence et al., 2007; Javadpour, 2009].
- (2) **Chemical and process industries:** The performance of porous catalysts depends critically on controlled gas transport, which governs reactant accessibility and overall reaction efficiency [Froment et al., 2010].
- (3) **Environmental engineering:** Gas flow behavior influences soil gas monitoring, landfill gas recovery, and carbon capture and sequestration, making an understanding of subsurface gas migration vital for environmental assessment and mitigation [Heid et al., 1950].
- (4) **Advanced technologies:** Gas transport through porous structures underlies the operation of fuel cells, filtration systems, insulation materials, and emerging micro- and nanofluidic devices, highlighting its cross-disciplinary relevance [Ho and Webb, 2006].

However, direct measurement of subsurface or internal flow behavior is often impractical or even impossible—particularly for gas transport—rendering experimental observations alone insufficient for fully understanding or predicting system dynamics [Bear, 2013; Dullien, 1992; Scheidegger, 1974]. In such circumstances, mathematical models become indispensable for estimating transport properties, evaluating system performance, simulating migration processes, and enabling efficient system design [Blunt, 2017; Lake et al., 2014; Whitaker, 1999]. Robust modeling frameworks help bridge the gap between laboratory-scale measurements and field-scale conditions by providing a systematic means to extrapolate controlled experimental data to complex natural environments [Bear, 2013; Bear and Cheng, 2010; Freeze and Cherry, 1979].

Numerous modeling strategies have been developed to describe gas transport in porous media across different length scales and flow regimes [Bear, 2013; Whitaker, 1986]. Classical continuum approaches—most notably the famous Darcy model—are valid for macroporous systems at sufficiently high pressures, corresponding to Knudsen numbers $\text{Kn} = \lambda/L < 10^{-3}$, where λ is the gas mean free path and L is a characteristic pore dimension. Under these conditions, the mean free path is much smaller than the pore size and the no-slip boundary condition applies [Bear, 2013]. As pressure decreases and the Knudsen number falls within the slip-flow regime ($10^{-3} \lesssim \text{Kn} \lesssim 10^{-1}$), molecule-wall interactions induce “rarefaction effects,” including velocity slip (a nonzero tangential velocity at the wall) and the breakdown of classical continuum assumptions [Beskok and Karniadakis, 1999]. Experiments show that, in this flow regime, the Darcy model underpredicts gas fluxes, yielding an apparent permeability greater than the intrinsic value [Javadpour, 2009]. To capture this non-Darcian behavior, models generally fall into two categories: non-continuum approaches that resolve microscale transport at higher Kn, and modified continuum frameworks that incorporate slip corrections while retaining macroscopic efficiency [Javadpour, 2009].

Within this family of continuum models, Klinkenberg [1941] proposed a widely used empirical correction that links apparent gas permeability to pressure. This modification enables continuum formulations to reproduce gas-transport behavior in low-pressure and tight-formation regimes, bridging idealized theory and experimental observations while avoiding costly pore-scale simulations. Incorporating the Klinkenberg effect makes the governing equations strongly nonlinear

and analytically intractable except in highly idealized settings. As a result, standard numerical methods—finite difference, finite volume, and finite element schemes—must employ iterative solvers (e.g., Newton–Raphson method) to handle the nonlinearity. These approaches often suffer from slow convergence and stability limitations due to the tight coupling between pressure and flow properties [Civan, 2010].

The field of gas transport in porous media would benefit from a modeling framework that satisfies the following design goals:

- G1.** Handle or mitigate convergence and stability issues inherent in nonlinear mathematical models.
- G2.** Achieve high accuracy in predicting the velocity field, which, in many applications, is as important as, or more important than, the pressure field.
- G3.** Exhibit strong numerical stability.

The central aim of this paper is to present such a modeling framework. To this end, we make several methodological choices and provide a rationale for each.

We begin by addressing design goal **G1**. Although originally developed to obtain analytical solutions for partial differential equations (PDEs) arising in heat conduction, the Hopf–Cole transformation offers an elegant way to overcome the computational challenges mentioned above: it introduces a suitable change of variables, converting a class of nonlinear partial differential equations into linear ones [Cole, 1951; Hopf, 1950; Vadasz, 2010]. In the realm of flow through porous media, a recent work by Maduri and Nakshatrala [2025] has demonstrated the efficacy of this transformation for models involving pressure-dependent fluid viscosity. Furthermore, they have shown that the transformation not only facilitates reliable numerical solutions but also simplifies mathematical analysis—including the establishment of qualitative properties such as maximum and comparison principles and the proof of solution uniqueness. Building on these developments, the present work extends the Hopf–Cole transformation to the Klinkenberg model, where nonlinearity arises from pressure-dependent permeability, thereby reformulating the governing flow equations into a more tractable linear form.

To address goal **G2**, which emphasizes accurate prediction of the velocity field, we adopt a mixed formulation implemented through a shared-trunk neural network architecture. Single-field formulations that solve for pressure alone and subsequently recover velocity by differentiation are well known to produce inaccurate or noisy velocity fields, particularly in heterogeneous porous media, where differentiation amplifies numerical errors and degrades local flux accuracy [Brezzi and Fortin, 1991; Raviart and Thomas, 1977]. For this reason, mixed formulations that solve for pressure and velocity simultaneously have long been recognized as essential for obtaining physically consistent and accurate velocity fields [Boffi et al., 2013]. However, when mixed formulations are implemented using separate neural networks for pressure and velocity, the resulting models often learn inconsistent latent representations, leading to reduced accuracy and loss of coupling between the predicted fields [Caruana, 1997; Ruder, 2017]. A shared-trunk architecture alleviates this issue by learning a common representation of the underlying flow physics while allowing task-specific output heads to specialize for pressure and velocity, thereby enforcing implicit coupling and improving the fidelity of the predicted velocity field [Karniadakis et al., 2021; Raissi et al., 2019].

To address goal **G3**, which calls for strong numerical stability, we adopt a *Deep Least-Squares* (DeepLS) formulation applied to the governing equations transformed into linear form via the

Hopf–Cole transformation. The unknown solution fields, represented by neural networks, are determined by minimizing a functional constructed directly from the governing equations and boundary conditions [Cai et al., 2020]. This formulation yields a nonnegative, symmetric, and positive-definite objective whose minimizer coincides with the solution of the underlying PDE system [Bersetche and Borthagaray, 2023]. When combined with the Hopf–Cole transformation, the method operates on linear Darcy-type equations rather than the original quasilinear system, resulting in a well-conditioned optimization landscape and a robust, meshfree solution strategy.

This stability stands in contrast to alternative physics-based deep learning approaches. The *Deep Ritz Method* requires the existence of a classical variational formulation [E and Yu, 2018; Manav et al., 2024; Samaniego et al., 2020]; while such a formulation exists for Darcy flow in mixed form through classical mixed Galerkin methods, the resulting stiffness matrix is a saddle-point system rather than positive definite, which poses challenges for numerical stability and solver robustness. *Physics-Informed Neural Networks* (PINNs), on the other hand, operate directly on strong-form PDE residuals and rely on collocation-based enforcement of the governing equations. Achieving stable training in PINNs often requires adaptive strategies for selecting collocation points and balancing loss terms, particularly in stiff or heterogeneous problems [Karniadakis et al., 2021; Raissi et al., 2019]. By contrast, DeepLS leverages least-squares formulations that inherently lead to symmetric and positive-definite operators, properties that are well known to ensure stability and robust performance of both linear and optimization solvers [Bersetche and Borthagaray, 2023; Cai et al., 2020]. These attributes make DeepLS particularly well suited for stable and reliable modeling of gas transport in porous media.

Thus, the proposed integrated modeling framework—combining a Klinkenberg-enhanced constitutive relation, Hopf–Cole–transformed linear PDEs in mixed form, a shared-trunk neural architecture, and a DeepLS-based solver—offers a robust and versatile approach for accurately modeling complex gas-transport phenomena in porous media. See **Fig. 1**.

The remainder of this paper is organized as follows. Section 2 formulates the boundary value problem for the Klinkenberg model. Section 3 introduces the integrated modeling framework, and Section 4 establishes its convergence properties. Section 5 presents numerical results that verify the accuracy and robustness of the proposed approach. In Section 6, a reciprocal relation is derived and utilized as an a posteriori error estimator to quantify solution accuracy. Finally, Section 7 summarizes the principal findings and contributions of the study.

2. MODEL INCORPORATING THE KLINKENBERG EFFECT

Consider the flow of a low-viscosity gas through a *rigid* porous medium. In our treatment of the flow, we do not resolve the motion of the gas at the pore scale. Instead, we work with a homogenized description at the macroscale, also referred to as the Darcy or plug–flow scale [Bear, 2013]. Accordingly, let $\Omega \subset \mathbb{R}^{nd}$ denote the macroscopic domain occupied by the porous medium, comprising both the solid matrix and the pore space; nd represents the number of spatial dimensions. The boundary of the domain is defined by

$$\partial\Omega := \overline{\Omega} \setminus \Omega \tag{2.1}$$

with $\overline{\Omega}$ denoting the closure of Ω [Evans, 1998].

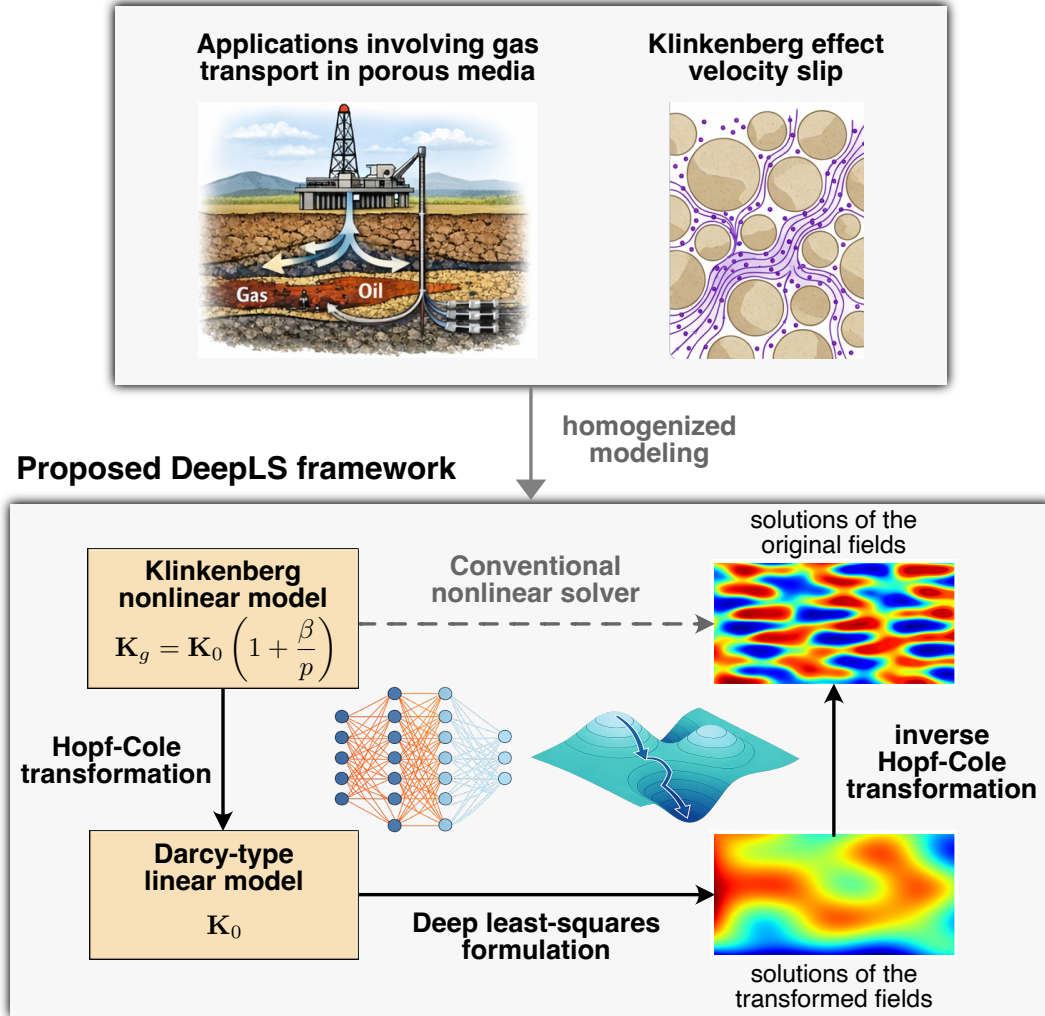


Figure 1. Conceptual framework and workflow of the proposed DeepLS framework. The nonlinear governing equations are reformulated via the Hopf–Cole transformation, yielding a linear system expressed in terms of a transformed pressure variable. A least-squares energy functional is then constructed for the resulting linear Darcy problem. The functional is minimized using a neural network–based deep least-squares formulation to compute the transformed pressure and velocity fields. Finally, the physical gas pressure is recovered through the inverse Hopf–Cole transformation, completing the solution procedure.

The domain is assumed to be bounded and to have a Lipschitz boundary.¹ By bounded, we mean that the domain is contained in a finite region of \mathbb{R}^{nd} . By Lipschitz, we mean that for each boundary point there exists a neighborhood and a coordinate system in which the set is locally given by the epigraph—the region lying above the graph—of a Lipschitz continuous function [Ziemer, 2012]. This condition permits non-smooth features such as corners and edges, while excluding pathological irregularities such as cusps or fractal boundaries, and it ensures the validity of standard analytical results for Sobolev spaces and partial differential equations [Adams and Fournier, 2003].

¹This assumption is imposed for technical reasons and is used in the convergence analysis; see Section 4.

A spatial point is written as $\mathbf{x} \in \bar{\Omega}$. The operators $\text{grad}[\cdot]$ and $\text{div}[\cdot]$ denote, respectively, the spatial gradient and divergence. The vector $\hat{\mathbf{n}}(\mathbf{x})$ denotes the outward-pointing unit normal on $\partial\Omega$. The Darcy (or discharge) velocity field is denoted by $\mathbf{u}(\mathbf{x})$, and the fluid² pressure is represented by $p(\mathbf{x})$. The intrinsic density and dynamic viscosity of the gas are denoted by γ and μ , respectively, while $\phi(\mathbf{x})$ denotes the local porosity, i.e., the volume fraction of pore space. Within a macroscopic (continuum-scale) description, one must specify the permeability field, which characterizes the effective ability of the porous medium to transmit fluid.

However, gas flow through a porous medium differs markedly from liquid flow. In particular, when a gas flows at sufficiently low pressures, slip at the pore walls becomes significant. Under these conditions, the classical no-slip boundary condition—typically valid for continuum-scale flows such as Stokes flow—no longer applies. This phenomenon, known as the *Klinkenberg slip effect*, leads to a distinction between the intrinsic (or absolute) permeability of the medium and the apparent gas permeability. In the Klinkenberg model, the apparent gas permeability (often referred to simply as the gas permeability) is defined as³

$$\mathbf{K}_g(\mathbf{x}) = \hat{\mathbf{K}}_g(\mathbf{x}, p(\mathbf{x})) = \mathbf{K}_0(\mathbf{x}) \left(1 + \frac{\beta p_{\text{atm}}}{p(\mathbf{x})} \right) \quad (2.2)$$

where $\hat{\mathbf{K}}_g(\mathbf{x}, p(\mathbf{x}))$ emphasizes the dependence of the gas permeability on both spatial position and gas pressure; $\mathbf{K}_0(\mathbf{x})$ denotes the intrinsic permeability field; $\beta \geq 0$ is the Klinkenberg parameter, which is dimensionless; and p_{atm} represents the atmospheric pressure. The intrinsic permeability field $\mathbf{K}_0(\mathbf{x})$ characterizes the influence of the pore geometry on flow within the porous medium. In the limit $p \rightarrow \infty$, the apparent permeability $\mathbf{K}_g(\mathbf{x})$ converges to the intrinsic permeability $\mathbf{K}_0(\mathbf{x})$, thereby recovering the standard Darcy model.

From physical considerations, the tensor $\mathbf{K}_0(\mathbf{x})$ is symmetric and strictly positive definite, and therefore invertible. Since the (absolute) pressure satisfies $p > 0$ and $\beta \geq 0$, and both are scalar quantities, the gas permeability tensor $\mathbf{K}_g(\mathbf{x})$ is likewise symmetric and positive definite. For mathematical analysis, we impose the stronger assumptions of uniform ellipticity and boundedness. Specifically, there exist constants k_{\min}, k_{\max} with $0 < k_{\min} \leq k_{\max}$ such that, for every $\mathbf{x} \in \Omega$ and for every nonzero vector $\boldsymbol{\zeta} \in \mathbb{R}^{nd}$ we have

$$k_{\min} \boldsymbol{\zeta} \bullet \boldsymbol{\zeta} \leq \boldsymbol{\zeta} \bullet \mathbf{K}_0(\mathbf{x}) \boldsymbol{\zeta} \leq k_{\max} \boldsymbol{\zeta} \bullet \boldsymbol{\zeta} \quad (2.3)$$

For an isotropic and spatially homogeneous porous medium, the intrinsic permeability reduces to the scalar form

$$\mathbf{K}_0(\mathbf{x}) = k_0 \mathbf{I} \quad (2.4)$$

where $k_0 > 0$ is a scalar permeability constant, and \mathbf{I} is the second-order identity tensor.

With regard to the boundary conditions, we split the boundary $\partial\Omega$ into two parts: Γ_u and Γ_p . Γ_u designates that portion of the boundary on which the normal component of the velocity is prescribed, while Γ_p is the portion on which pressure is prescribed. For mathematical well-posedness, we require:

$$\Gamma_u \cup \Gamma_p = \partial\Omega \quad \text{and} \quad \Gamma_u \cap \Gamma_p = \emptyset \quad (2.5)$$

We assume that Γ_p is of positive measure, that is, $\text{meas}(\Gamma_p) > 0$.

²Throughout this paper, the term *fluid* refers exclusively to a gas. Since liquids are not considered, there should be no confusion with the usage.

³See Remark 2.

The governing equations for gas flow through porous media under the Klinkenberg model take the following form:

$$\mu(\mathbf{x}) \widehat{\mathbf{K}}_g^{-1}(\mathbf{x}, p(\mathbf{x})) \mathbf{u}(\mathbf{x}) + \text{grad}[p(\mathbf{x})] = \phi(\mathbf{x}) \gamma \mathbf{b}(\mathbf{x}) \approx \mathbf{0} \quad \text{in } \Omega \quad (2.6a)$$

$$\text{div}[\mathbf{u}(\mathbf{x})] = 0 \quad \text{in } \Omega \quad (2.6b)$$

$$\mathbf{u}(\mathbf{x}) \bullet \widehat{\mathbf{n}}(\mathbf{x}) = u_n(\mathbf{x}) \quad \text{on } \Gamma_u \quad (2.6c)$$

$$p(\mathbf{x}) = p_p(\mathbf{x}) \quad \text{on } \Gamma_p \quad (2.6d)$$

where $\mathbf{b}(\mathbf{x})$ is the specific body force, $u_n(\mathbf{x})$ is the normal component of the (Darcy) velocity prescribed on the boundary, and $p_p(\mathbf{x})$ is the pressure prescribed on the boundary.

In Eq. (2.6a), the gas density is generally small, particularly under low-pressure conditions. As a result, the contribution of the body-force term $\phi(\mathbf{x})\gamma\mathbf{b}(\mathbf{x})$ is negligible compared to the pressure-gradient term, and it is therefore omitted in the subsequent analysis.

The parameter β depends strongly on the pore structure of the porous medium and on the type of gas. Table 1 reports typical ranges of β for various porous materials; these values primarily reflect differences in pore structure and do not account for the specific gas employed. Larger values of β correspond to stronger gas-slippage effects and are particularly significant in tight formations such as shale. Since the gas permeability depends on the pressure, the above boundary-value problem is therefore *nonlinear*.

A few remarks are in order before we present the proposed modeling framework.

Remark 1. When the boundary partition assigns the entire boundary $\partial\Omega$ to the flux (i.e., $\Gamma_u = \partial\Omega$), the boundary data $u_n(\mathbf{x}) := \mathbf{u}(\mathbf{x}) \bullet \widehat{\mathbf{n}}(\mathbf{x})$ cannot be prescribed arbitrarily. Since the velocity field is solenoidal in Ω , the net volumetric flow across the boundary must vanish [Schey, 2005]. Consequently, the boundary flux must satisfy

$$\int_{\partial\Omega} u_n(\mathbf{x}) \, d\Gamma = 0 \quad (2.7)$$

This follows by integrating $\text{div}[\mathbf{u}(\mathbf{x})] = 0$ over Ω and invoking Gauss' theorem:

$$0 = \int_{\Omega} \text{div}[\mathbf{u}(\mathbf{x})] \, d\Omega = \int_{\partial\Omega} \mathbf{u}(\mathbf{x}) \bullet \widehat{\mathbf{n}}(\mathbf{x}) \, d\Gamma = \int_{\partial\Omega} u_n(\mathbf{x}) \, d\Gamma \quad (2.8)$$

which coincides with Eq. (2.7).

Remark 2. In the existing literature, the Klinkenberg model is most commonly expressed in the following scalar form:

$$K_g = k_0 \left(1 + \frac{\beta}{p} \right) \quad (2.9)$$

In this formulation, the parameter β has the dimensions of pressure. By contrast, in the formulation adopted in the present work, β is dimensionless. Moreover, the proposed framework extends the classical Klinkenberg model by permitting the permeability to be anisotropic and spatially inhomogeneous.

3. PROPOSED MODELING FRAMEWORK

This section presents an integrated modeling framework that couples the Hopf–Cole transformation with a least-squares energy functional–based deep neural network. The workflow of the

Table 1. Typical values of the Klinkenberg parameter β .

| Rock type | Typical β |
|----------------------|-----------------|
| Glass bead packs | ≈ 0 |
| Metal-ceramic foams | ≈ 0 |
| Coarse-grained sands | 0–0.5 |
| Carbonates | 1–10 |
| Tight sandstone | 2–20 |
| Shale | 10–200 |

proposed framework—referred to as the **DeepLS framework**—is summarized in the following four steps (see Fig. 1):

- Step 1.** Apply the Hopf–Cole transformation to recast the nonlinear governing equations into a linear system in the transformed pressure variable;
- Step 2.** Construct a least-squares energy functional associated with the resulting linear Darcy problem;
- Step 3.** Minimize the energy functional numerically using a neural network–based deep least-squares method to solve the linear Darcy problem and obtain the transformed pressure and velocity fields; and
- Step 4.** Recover the physical gas pressure by applying the inverse Hopf–Cole transformation.

The remainder of this section elaborates on each step of the proposed workflow.

3.1. Hopf–Cole transformation. We introduce a transformed scalar pressure variable defined by

$$\mathcal{P}(\mathbf{x}) := \int \left(1 + \frac{\beta p_{\text{atm}}}{p} \right) dp = p(\mathbf{x}) + \beta p_{\text{atm}} \ln[p(\mathbf{x})] \quad (3.1)$$

Taking the spatial gradient of both sides yields

$$\text{grad}[\mathcal{P}(\mathbf{x})] = \left(1 + \frac{\beta p_{\text{atm}}}{p(\mathbf{x})} \right) \text{grad}[p(\mathbf{x})] \quad (3.2)$$

Notably, the velocity field remains unchanged under this transformation. Consequently, when expressed in terms of the variables $\mathbf{u}(\mathbf{x})$ and $\mathcal{P}(\mathbf{x})$, the governing equations take the following linear form:

$$\mu \mathbf{K}_0^{-1}(\mathbf{x}) \mathbf{u}(\mathbf{x}) + \text{grad}[\mathcal{P}(\mathbf{x})] = \mathbf{0} \quad \text{in } \Omega \quad (3.3a)$$

$$\text{div}[\mathbf{u}(\mathbf{x})] = 0 \quad \text{in } \Omega \quad (3.3b)$$

$$\mathbf{u}(\mathbf{x}) \bullet \hat{\mathbf{n}}(\mathbf{x}) = u_n(\mathbf{x}) \quad \text{on } \Gamma_u \quad (3.3c)$$

$$\mathcal{P}(\mathbf{x}) = \mathcal{P}_p(\mathbf{x}) \quad \text{on } \Gamma_p \quad (3.3d)$$

Here, the prescribed pressure boundary condition expressed in terms of the transformed pressure variable is given by

$$\mathcal{P}_p(\mathbf{x}) := p_p(\mathbf{x}) + \beta p_{\text{atm}} \ln[p_p(\mathbf{x})] \quad (3.4)$$

The governing equations expressed in terms of the transformed pressure variable $\mathcal{P}(\mathbf{x})$ are linear (cf. Eqs. (3.3a)–(3.3d)). It is worth noting that the transformation leading to linearity is not unique. For example, adding an arbitrary constant to the right-hand side of Eq. (3.1) leaves Eq. (3.2) unchanged and therefore results in the same linear governing equations. Additional discussion of Hopf–Cole transformations in porous-media flow can be found in Maduri and Nakshatrala [2025]. Also, see the discussion in Vadasz [2010].

We note that the logarithmic structure of the transformation imposes admissibility constraints on the prescribed pressure data, which are discussed next.

Remark 3 (Admissibility of prescribed pressure data). A point of caution is necessary regarding the prescribed pressure $p_p(\mathbf{x})$. In the physical setting considered here, the pressure represents an *absolute* gas pressure and is therefore strictly positive. Under this assumption, the Hopf–Cole transformation employed in the Klinkenberg model, which involves a logarithmic dependence as shown in Eq. (3.4), is well-defined.

However, care must be exercised when applying nondimensionalization or when redefining the pressure datum. In particular, shifting the reference pressure or rescaling the pressure field may result in values that are zero or negative, even if the underlying physical pressure remains positive. In such cases, the Hopf–Cole transformation ceases to be applicable, since the logarithmic mapping is no longer meaningful.

Consequently, the present formulation requires the use of strictly positive absolute pressures. When this condition is satisfied, no additional restrictions arise from the transformation. In all numerical tests and implementations, we therefore enforce

$$p_p(\mathbf{x}) \geq p_{\min} > 0 \quad \text{on } \Gamma_p \quad (3.5)$$

where p_{\min} is a small positive threshold chosen consistently with the physical operating range.

3.2. Least-squares functional. We define the following residuals corresponding to the governing equations and boundary conditions:

$$\mathbf{R}_1 := \mu \mathbf{K}_0^{-1}(\mathbf{x}) \mathbf{u}(\mathbf{x}) + \text{grad}[\mathcal{P}(\mathbf{x})] \quad (3.6a)$$

$$\mathbf{R}_2 := \text{div}[\mathbf{u}(\mathbf{x})] \quad (3.6b)$$

$$\mathbf{R}_3 := \mathbf{u}(\mathbf{x}) \cdot \hat{\mathbf{n}}(\mathbf{x}) - u_n(\mathbf{x}) \quad (3.6c)$$

$$\mathbf{R}_4 := \mathcal{P}(\mathbf{x}) - \mathcal{P}_p(\mathbf{x}) \quad (3.6d)$$

Here, the residual \mathbf{R}_1 is vector-valued and is therefore typeset in boldface, whereas the residuals \mathbf{R}_2 , \mathbf{R}_3 , and \mathbf{R}_4 are scalar-valued. The residuals \mathbf{R}_1 and \mathbf{R}_2 are defined over the domain Ω , while \mathbf{R}_3 and \mathbf{R}_4 are defined on the boundary segments Γ_u and Γ_p , respectively.

To address the mixed saddle-point structure of the system defined by Eqs. (3.6a)–(3.6d), we introduce the following weighted least-squares functional:

$$\Pi_{\text{LS}}[\mathcal{P}(\mathbf{x}), \mathbf{u}(\mathbf{x})] := \frac{1}{2} \|\mu^{-1/2} \sqrt{\mathbf{K}_0(\mathbf{x})} \mathbf{R}_1\|_{\Omega}^2 + \frac{1}{2} \|\mathbf{R}_2\|_{\Omega}^2 + \frac{1}{2} \|\mathbf{R}_3\|_{\Gamma_u}^2 + \frac{1}{2} \|\mathbf{R}_4\|_{\Gamma_p}^2 \quad (3.7)$$

Here, $\|\cdot\|_K$ denotes the L^2 -norm over the set K , defined by

$$\|v\|_K^2 := \int_K v \cdot v \, dK \quad (3.8)$$

with $K = \Omega$, Γ_u , or Γ_p as appropriate. For scalar-valued quantities, $v \cdot v$ reduces to v^2 .

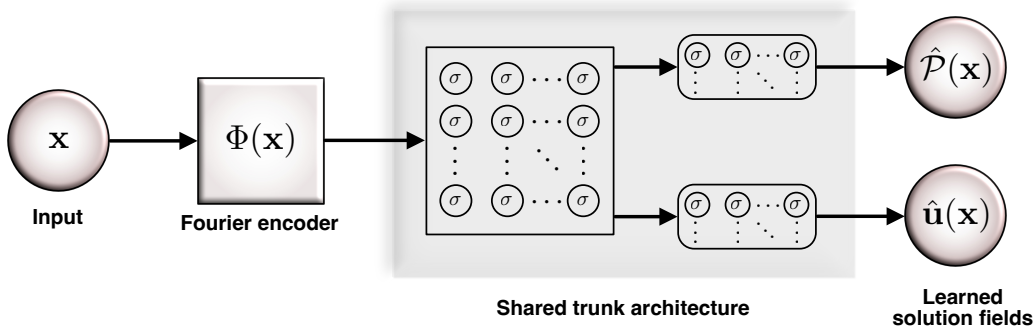


Figure 2. The figure shows the neural network architecture used under the DeepLS framework.

Equivalently, the least-squares functional may be expressed in integral form as

$$\begin{aligned} \Pi_{\text{LS}}[\mathcal{P}(\mathbf{x}), \mathbf{u}(\mathbf{x})] &= \frac{1}{2} \int_{\Omega} \left(\mu^{-1/2} \sqrt{\mathbf{K}_0(\mathbf{x})} \mathbf{R}_1(\mathbf{x}) \right) \bullet \left(\mu^{-1/2} \sqrt{\mathbf{K}_0(\mathbf{x})} \mathbf{R}_1(\mathbf{x}) \right) d\Omega \\ &\quad + \frac{1}{2} \int_{\Omega} (R_2(\mathbf{x}))^2 d\Omega + \frac{1}{2} \int_{\Gamma_u} (R_3(\mathbf{x}))^2 d\Gamma + \frac{1}{2} \int_{\Gamma_p} (R_4(\mathbf{x}))^2 d\Gamma \end{aligned} \quad (3.9)$$

3.3. DeepLS neural network approximation. We now present the neural network framework for solving the transformed linear Darcy problem given in Eqs. (3.3a)–(3.3d) which is carried out by minimizing the energy functional given in Eq. (3.9). **Figure 2** illustrates the shared-trunk neural network architecture employed within the DeepLS framework, and the main components of the construction are summarized below. A detailed description of the shared-trunk architecture in the context of multi-field problems can be found in [Maduri and Nakshatrala \[2026\]](#).

3.3.1. *Neural representation of the solution fields.* Let \mathcal{N}_{θ} be a neural network with trainable parameters θ . We approximate the transformed pressure and Darcy velocity as

$$(\mathcal{P}(\mathbf{x}), \mathbf{u}(\mathbf{x})) \approx (\mathcal{P}_{\theta}(\mathbf{x}), \mathbf{u}_{\theta}(\mathbf{x})) := \mathcal{N}_{\theta}(\mathbf{x}) \quad \mathbf{x} \in \Omega \quad (3.10)$$

In practice we employ a shared trunk neural network architecture followed by two output heads: a scalar head for \mathcal{P}_{θ} and a vector head for \mathbf{u}_{θ} . To improve expressivity for heterogeneous/steep fields, the spatial coordinates are first lifted using a Fourier-feature map

$$\phi(\mathbf{x}) = \left[\mathbf{x}, \sin(\omega_1 \mathbf{x}), \cos(\omega_1 \mathbf{x}), \dots, \sin(\omega_{n_f} \mathbf{x}), \cos(\omega_{n_f} \mathbf{x}) \right] \quad (3.11)$$

where $\{\omega_k\}$ are fixed frequencies. The network is thus evaluated as $\mathcal{N}_{\theta}(\mathbf{x}) = \tilde{\mathcal{N}}_{\theta}(\phi(\mathbf{x}))$. Given the parametric approximations $(\mathcal{P}_{\theta}(\mathbf{x}), \mathbf{u}_{\theta}(\mathbf{x}))$, the residuals $\mathbf{R}_1, R_2, R_3, R_4$ defined in Eqs. (3.6a)–(3.6d) are obtained by replacing $(\mathcal{P}(\mathbf{x}), \mathbf{u}(\mathbf{x}))$ with their parametric counterparts. All required spatial derivatives are evaluated using automatic differentiation.

3.3.2. *Monte Carlo approximation of the least-squares functional.* The least-squares functional Π defined in Eq. (3.9) involves integrals over the domain Ω and the boundary segments Γ_u and Γ_p . These integrals are approximated using Monte Carlo quadrature based on three sets of collocation points:

$$\mathcal{X}_{\Omega} = \{\mathbf{x}_{\Omega}^{(i)}\}_{i=1}^{N_{\Omega}} \subset \Omega, \quad \mathcal{X}_u = \{\mathbf{x}_u^{(j)}\}_{j=1}^{N_u} \subset \Gamma_u, \quad \text{and} \quad \mathcal{X}_p = \{\mathbf{x}_p^{(k)}\}_{k=1}^{N_p} \subset \Gamma_p \quad (3.12)$$

Using these point clouds, the squared norms appearing in the functional are approximated by sample averages, optionally scaled by the geometric measures $|\Omega|$, $|\Gamma_u|$, and $|\Gamma_p|$. These geometric factors may equivalently be absorbed into the corresponding weighting parameters. The resulting empirical DeepLS objective is given by

$$\widehat{\Pi}_{\text{LS}}(\boldsymbol{\theta}) = \lambda_1 \widehat{\Pi}_1(\boldsymbol{\theta}) + \lambda_2 \widehat{\Pi}_2(\boldsymbol{\theta}) + \lambda_3 \widehat{\Pi}_3(\boldsymbol{\theta}) + \lambda_4 \widehat{\Pi}_4(\boldsymbol{\theta}) \quad (3.13a)$$

$$\widehat{\Pi}_1(\boldsymbol{\theta}) = \frac{1}{2N_\Omega} \sum_{i=1}^{N_\Omega} \left\| \mu^{-1/2} \sqrt{\mathbf{K}_0(\mathbf{x}_\Omega^{(i)})} \mathbf{R}_{1,\boldsymbol{\theta}}(\mathbf{x}_\Omega^{(i)}) \right\|_2^2 \quad (3.13b)$$

$$\widehat{\Pi}_2(\boldsymbol{\theta}) = \frac{1}{2N_\Omega} \sum_{i=1}^{N_\Omega} \left(R_{2,\boldsymbol{\theta}}(\mathbf{x}_\Omega^{(i)}) \right)^2 \quad (3.13c)$$

$$\widehat{\Pi}_3(\boldsymbol{\theta}) = \frac{1}{2N_u} \sum_{j=1}^{N_u} \left(R_{3,\boldsymbol{\theta}}(\mathbf{x}_u^{(j)}) \right)^2 \quad (3.13d)$$

$$\widehat{\Pi}_4(\boldsymbol{\theta}) = \frac{1}{2N_p} \sum_{k=1}^{N_p} \left(R_{4,\boldsymbol{\theta}}(\mathbf{x}_p^{(k)}) \right)^2 \quad (3.13e)$$

Here, $\mathbf{R}_{1,\boldsymbol{\theta}}$, $R_{2,\boldsymbol{\theta}}$, $R_{3,\boldsymbol{\theta}}$, and $R_{4,\boldsymbol{\theta}}$ denote the residuals evaluated using the neural-network approximations of the solution fields. The DeepLS approximation is obtained by solving the following optimization problem:

$$\boldsymbol{\theta}^* = \arg \min_{\boldsymbol{\theta}} \widehat{\Pi}_{\text{LS}}(\boldsymbol{\theta}) \quad (3.14)$$

3.3.3. Adaptive loss weighting. The four contributions in Eq. (3.13) may differ significantly in both magnitude and convergence behavior. To prevent the training process from being dominated by a single term—such as boundary-condition residuals overwhelming interior PDE residuals, or vice versa—we adaptively update the weights $\{\lambda_m\}_{m=1}^4$ during training.

Let $L_m^{(t)}$ denote the value of the empirical loss component $\widehat{\Pi}_m$ at training iteration t . We monitor the relative decrease

$$r_m^{(t)} = \left| \frac{L_m^{(t-1)} - L_m^{(t)}}{L_m^{(t-1)} + \varepsilon} \right| \quad (3.15)$$

and compute a moving average \bar{r}_m over a short window of iterations. When the ratio

$$\max_m \bar{r}_m / \min_m \bar{r}_m$$

exceeds a prescribed threshold, the weights are rebalanced so that more slowly converging terms receive increased emphasis.

One convenient update rule for the adaptive loss weights is

$$\lambda_m \leftarrow 1 + \alpha \frac{\bar{r}_{\max} - \bar{r}_m}{\bar{r}_{\max} - \bar{r}_{\min} + \varepsilon} \quad (3.16)$$

where $\bar{r}_{\max} := \max_m \bar{r}_m$ and $\bar{r}_{\min} := \min_m \bar{r}_m$. The parameter $\alpha > 0$ controls the strength of the reweighting, while $\varepsilon \ll 1$ is a small regularization constant introduced to ensure numerical stability. This adaptive weighting strategy is lightweight, requires no additional backpropagation passes, and has been observed to stabilize training in the presence of multiple competing loss terms.

3.3.4. *Optimization strategy.* Due to the neural-network parameterization, the DeepLS objective defined in Eq. (3.13) depends nonlinearly on the parameter vector $\boldsymbol{\theta}$. We therefore employ a two-stage optimization strategy.

In the first stage, a stochastic first-order optimizer (Adam) is used to rapidly decrease the objective starting from random initialization, using mini-batches of interior collocation points. In the second stage, we switch to a (quasi-)Newton method (L-BFGS) to obtain a high-accuracy solution once the iterates approach a minimizer. In addition, gradient clipping and a learning-rate scheduler may be employed to further enhance robustness and convergence stability.

3.4. Inverse transformation. After solving the transformed problem for the auxiliary pressure variable $\mathcal{P}(\mathbf{x})$, the original physical gas pressure $p(\mathbf{x})$ is recovered by inverting the Hopf–Cole transformation. When $p(\mathbf{x})$ is interpreted as an absolute pressure, it satisfies $p(\mathbf{x}) > 0$. On this domain, the mapping $p \mapsto \mathcal{P} = p + \beta p_{\text{atm}} \ln[p]$ is continuous and strictly monotone for $\beta \geq 0$, which ensures a one-to-one correspondence between p and \mathcal{P} . Consequently, the transformation is invertible on the interval $(0, \infty)$.

The inverse mapping can be expressed in closed form using the Lambert– W function [Corless et al., 1996], defined as the solution of $W(z)e^{W(z)} = z$. Applying this definition to the Hopf–Cole transformation yields

$$p(\mathbf{x}) = \beta p_{\text{atm}} W\left(\frac{1}{\beta p_{\text{atm}}} \exp\left(\frac{\mathcal{P}(\mathbf{x})}{\beta p_{\text{atm}}}\right)\right) \quad (3.17)$$

which provides an explicit expression for the physical pressure in terms of the transformed variable. For the positive-pressure regime considered here, the principal branch of the Lambert– W function is used.

4. CONVERGENCE ANALYSIS

4.1. Notation and function analytic setting. We now enumerate the assumptions underpinning the subsequent mathematical analysis:

- (i) $\Omega \subset \mathbb{R}^{nd}$ is a bounded Lipschitz domain.
- (ii) The coefficient of viscosity satisfies $\mu > 0$.
- (iii) The permeability is an essentially bounded (i.e., $\mathbf{K}(\mathbf{x}) \in L^\infty(\Omega; \mathbb{R}^{nd \times nd})$) and uniformly elliptic. That is, there exist $0 < k_{\min} \leq k_{\max} < \infty$ such that

$$k_{\min} \|\boldsymbol{\xi}\|^2 \leq \boldsymbol{\xi} \bullet \mathbf{K}(\mathbf{x}) \boldsymbol{\xi} \leq k_{\max} \|\boldsymbol{\xi}\|^2, \quad \text{for a.e. } \mathbf{x} \in \Omega, \forall \boldsymbol{\xi} \in \mathbb{R}^{nd} \quad (4.1)$$

Furthermore, the permeability is symmetric.

- (iv) The pressure is prescribed on a subset of the boundary of positive measure: $\text{meas}(\Gamma_p) > 0$. This condition fixes the pressure datum.

The set of trial functions—that is, solution fields—is written as follows:

$$\mathbb{U}(\mathbf{x}) = \left\{ \begin{array}{c} \mathcal{P}(\mathbf{x}) \\ \mathbf{u}(\mathbf{x}) \end{array} \right\} \quad (4.2)$$

Similarly, the associated test (or weighting) functions are collectively represented as follows:

$$\mathbb{W}(\mathbf{x}) = \left\{ \begin{array}{c} q(\mathbf{x}) \\ \mathbf{w}(\mathbf{x}) \end{array} \right\} \quad (4.3)$$

An explanation of the choice of appropriate function spaces for the individual solution fields is required to ensure that all terms appearing in the least-squares functional, including boundary contributions, are well defined.

The pressure field may be taken in the Sobolev space $H^1(\Omega)$. By the trace theorem for scalar H^1 functions [Evans, 1998], this choice ensures that

$$\text{trace}(p(\mathbf{x})) \in H^{1/2}(\partial\Omega) \subset L^2(\partial\Omega) \quad (4.4)$$

provided the boundary $\partial\Omega$ is sufficiently regular (e.g., Lipschitz), which is the case in this paper. Consequently, $p(\mathbf{x}) \in H^1(\Omega)$ guarantees that all least-squares terms involving the pressure, both in the domain Ω and on the boundary Γ_p , are well defined.

Since the velocity boundary condition is enforced weakly, the standard Sobolev space $H(\text{div}; \Omega)$ [Brenner and Scott, 2008] is not sufficient for the velocity field. Indeed, if $\mathbf{u} \in H(\text{div}; \Omega)$, then only the normal component of the trace is well defined, and it satisfies

$$\text{trace}(\mathbf{u}(\mathbf{x})) = \mathbf{u}(\mathbf{x}) \bullet \hat{\mathbf{n}}(\mathbf{x}) \in H^{-1/2}(\partial\Omega) \quad (4.5)$$

which is a dual space and may contain distributions rather than functions. Moreover, for a Lipschitz boundary $\partial\Omega$, we have

$$L^2(\partial\Omega) \subset H^{-1/2}(\partial\Omega) \quad (4.6)$$

with a continuous embedding. Furthermore, the natural norm on $H^{-1/2}(\partial\Omega)$ is not the $L^2(\partial\Omega)$ norm. However, in the present formulation the velocity boundary conditions are enforced via a least-squares term measured in the $L^2(\partial\Omega)$ norm. Consequently, a stronger function space for the velocity field is required—one that guarantees an L^2 -integrable boundary trace. We, thus, require $\mathbf{u}(\mathbf{x}) \in H(\text{div}; \Omega, \Gamma_u)$ where

$$H(\text{div}; \Omega, \Gamma_u) := \left\{ \mathbf{u}(\mathbf{x}) \in H(\text{div}; \Omega) \mid \mathbf{u}(\mathbf{x}) \bullet \hat{\mathbf{n}}(\mathbf{x}) \in L^2(\Gamma_u) \right\} \quad (4.7)$$

Therefore, the appropriate product function space for $\mathbb{U}(\mathbf{x})$ is

$$\mathcal{U} = H^1(\Omega) \times H(\text{div}; \Omega, \Gamma_u) \quad (4.8)$$

The natural inner product of \mathcal{U} is

$$\begin{aligned} (\mathbb{W}(\mathbf{x}); \mathbb{U}(\mathbf{x}))_{\mathcal{U}} &:= \int_{\Omega} q(\mathbf{x}) \mathcal{P}(\mathbf{x}) \, d\Omega + \int_{\Omega} \text{grad}[q(\mathbf{x})] \bullet \text{grad}[\mathcal{P}(\mathbf{x})] \, d\Omega \\ &\quad + \int_{\Omega} \mathbf{w}(\mathbf{x}) \bullet \mathbf{u}(\mathbf{x}) \, d\Omega + \int_{\Omega} \text{div}[\mathbf{w}(\mathbf{x})] \text{div}[\mathbf{u}(\mathbf{x})] \, d\Omega \\ &\quad + \int_{\Gamma_u} \left(\mathbf{w}(\mathbf{x}) \bullet \hat{\mathbf{n}}(\mathbf{x}) \right) \left(\mathbf{u}(\mathbf{x}) \bullet \hat{\mathbf{n}}(\mathbf{x}) \right) \, d\Gamma \end{aligned} \quad (4.9)$$

The associated norm is

$$\begin{aligned} \|\mathbb{U}(\mathbf{x})\|_{\mathcal{U}}^2 &:= (\mathbb{U}(\mathbf{x}); \mathbb{U}(\mathbf{x}))_{\mathcal{U}} \equiv \|\mathcal{P}(\mathbf{x})\|_{H^1(\Omega)}^2 + \|\mathbf{u}(\mathbf{x})\|_{H(\text{div}; \Omega, \Gamma_u)}^2 \\ &= \|\mathcal{P}(\mathbf{x})\|_{H^1(\Omega)}^2 + \|\mathbf{u}(\mathbf{x})\|_{H(\text{div}; \Omega)}^2 + \|\mathbf{u}(\mathbf{x}) \bullet \hat{\mathbf{n}}(\mathbf{x})\|_{L^2(\Gamma_u)}^2 \end{aligned} \quad (4.10)$$

We now establish that \mathcal{U} is a Hilbert space under the inner product defined in Eq. (4.9). We first note that $H^1(\Omega)$ is a Hilbert space under its standard inner product [Adams and Fournier, 2003], corresponding to the first two terms on the right-hand side of Eq. (4.9).

Moreover, $H(\text{div}; \Omega)$ endowed with its graph inner product is a Hilbert space [Girault and Raviart, 1986]. Since the normal trace operator from $H(\text{div}; \Omega)$ into $H^{-1/2}(\partial\Omega)$ is continuous and

$L^2(\Gamma_u)$ is continuously embedded in $H^{-1/2}(\Gamma_u)$, the induced graph norm $\|\cdot\|_{H(\text{div};\Omega,\Gamma_u)}$ is complete [Adams and Fournier, 2003; Monk, 2003]. Hence, $H(\text{div};\Omega,\Gamma_u)$ is also a Hilbert space under the induced inner product, corresponding to the last three terms in Eq. (4.9).

It then follows that the Cartesian product

$$\mathcal{U} = H^1(\Omega) \times H(\text{div};\Omega,\Gamma_u),$$

endowed with the sum inner product given by Eq. (4.9), is itself a Hilbert space [Brezis, 2011].

Remark 4 (Alternative regularity assumptions for the flux). A brief comment on alternatives to the space $H(\text{div};\Omega,\Gamma_u)$ and their implications for the least-squares construction is in order. The space $H(\text{div};\Omega,\Gamma_u)$ is introduced because the velocity boundary residual is measured in the $L^2(\Gamma_u)$ norm, which requires adequate control of the normal trace.

One possibility is to retain the minimal regularity $\mathbf{u} \in H(\text{div};\Omega)$ and measure the boundary residual in the dual norm $H^{-1/2}(\Gamma_u)$ by incorporating the corresponding term in the least-squares functional. This avoids strengthening the trial space but introduces dual norms and duality pairings. The role of negative-order trace spaces for Darcy flux data and the distinction between natural $H^{-1/2}$ traces and L^2 -based weak enforcement are discussed in Burman and Puppi [2022].

At the other extreme, one may assume stronger bulk regularity, $\mathbf{u}(\mathbf{x}) \in [H^1(\Omega)]^d$, which implies $\mathbf{u}(\mathbf{x}) \bullet \hat{\mathbf{n}}(\mathbf{x}) \in H^{1/2}(\Gamma_u) \subset L^2(\Gamma_u)$ and thus makes an $L^2(\Gamma_u)$ boundary penalty automatically well defined. However, this exceeds what is required for mixed Darcy formulations and can be restrictive for heterogeneous coefficients or low-regularity flux data.

The present approach balances these alternatives: it preserves the natural $H(\text{div};\Omega)$ conformity of mixed formulations while ensuring that the $L^2(\Gamma_u)$ boundary least-squares term is well defined and directly controlled in the induced norm. Augmenting $H(\text{div};\Omega)$ with explicit $L^2(\Gamma_u)$ control of the normal trace therefore yields a consistent and flexible functional framework, in line with Bernkopf and Melenk [2024].

4.1.1. *Useful inequalities.* We next recall several inequalities that will be used repeatedly in the analysis. The trace theorem for scalar functions in $H^1(\Omega)$ implies the existence of a constant $C_{\text{tr}} > 0$, depending only on Ω and Γ_p , such that

$$\|p(\mathbf{x})\|_{L^2(\Gamma_p)} \leq C_{\text{tr}} \|p(\mathbf{x})\|_{H^1(\Omega)} \quad (4.11)$$

The Friedrichs-Poincaré inequality, combined with the trace theorem for scalar functions in $H^1(\Omega)$, yields the estimate

$$\|p(\mathbf{x})\|_{L^2(\Omega)} \leq C_P \left(\|\text{grad}[p(\mathbf{x})]\|_{L^2(\Omega)} + \|p(\mathbf{x})\|_{L^2(\Gamma_p)} \right) \quad (4.12)$$

Expressing this bound in square form, and invoking the Cauchy–Schwarz (or equivalently $(a+b)^2 \leq 2(a^2 + b^2)$) inequality, we obtain

$$\|p(\mathbf{x})\|_{L^2(\Omega)}^2 \leq 2C_P^2 \left(\|\text{grad}[p(\mathbf{x})]\|_{L^2(\Omega)}^2 + \|p(\mathbf{x})\|_{L^2(\Gamma_p)}^2 \right) \quad (4.13)$$

In square form, the Friedrichs inequality for vector fields in $H(\text{div};\Omega,\Gamma_u)$ takes the following form:

$$\|\mathbf{u}(\mathbf{x})\|_{L^2(\Omega)}^2 \leq 2C_{\text{div}}^2 \left(\|\text{div}[\mathbf{u}(\mathbf{x})]\|_{L^2(\Omega)}^2 + \|\mathbf{u}(\mathbf{x}) \bullet \mathbf{n}(\mathbf{x})\|_{L^2(\Gamma_u)}^2 \right) \quad (4.14)$$

Proofs of the above inequalities can be found in Adams and Fournier [2003]; Girault and Raviart [1986]; Lions and Magenes [1972].

4.1.2. *Bilinear form and linear functional.* With the functional setting established, we define the bilinear form and its associated linear functional. The bilinear form is given by

$$\begin{aligned} \mathcal{B}(\mathbb{W}(\mathbf{x}); \mathbb{U}(\mathbf{x})) &:= \int_{\Omega} \left(\mu \mathbf{K}_0^{-1}(\mathbf{x}) \mathbf{w}(\mathbf{x}) + \text{grad}[q(\mathbf{x})] \right) \bullet \frac{1}{\mu} \mathbf{K}_0(\mathbf{x}) \left(\mu \mathbf{K}_0^{-1}(\mathbf{x}) \mathbf{u}(\mathbf{x}) + \text{grad}[\mathcal{P}(\mathbf{x})] \right) d\Omega \\ &\quad + \int_{\Omega} \text{div}[\mathbf{w}(\mathbf{x})] \text{div}[\mathbf{u}(\mathbf{x})] d\Omega + \int_{\Gamma_u} \left(\mathbf{w}(\mathbf{x}) \bullet \hat{\mathbf{n}}(\mathbf{x}) \right) \left(\mathbf{u}(\mathbf{x}) \bullet \hat{\mathbf{n}}(\mathbf{x}) \right) d\Gamma \\ &\quad + \int_{\Gamma_p} q(\mathbf{x}) \mathcal{P}(\mathbf{x}) d\Gamma \end{aligned} \quad (4.15)$$

The linear functional is defined as follows:

$$l(\mathbb{W}(\mathbf{x})) := \int_{\Gamma_u} \left(\mathbf{w}(\mathbf{x}) \bullet \hat{\mathbf{n}}(\mathbf{x}) \right) u_n(\mathbf{x}) d\Gamma + \int_{\Gamma_p} q(\mathbf{x}) \mathcal{P}_p(\mathbf{x}) d\Gamma \quad (4.16)$$

The *infinite-dimensional optimization problem* can be stated as follows:

$$\inf_{\mathbb{U}(\mathbf{x}) \in \mathcal{U}} \Pi_{\text{LS}}[\mathbb{U}(\mathbf{x})] \quad (4.17)$$

The associated *least-squares objective functional* is defined as

$$\Pi_{\text{LS}}[\mathbb{U}(\mathbf{x})] := \frac{1}{2} \mathcal{B}(\mathbb{U}(\mathbf{x}); \mathbb{U}(\mathbf{x})) - l(\mathbb{U}(\mathbf{x})) \quad (4.18)$$

4.2. Minimizers, total error, and error decomposition. In addition to the ambient solution space \mathcal{U} , the analysis involves a network class $\mathcal{N} \subset \mathcal{U}$, representing the set of admissible neural network approximations.

Let $\mathcal{N}_p \subset H^1(\Omega)$ and $\mathcal{N}_u \subset H(\text{div}; \Omega, \Gamma_u)$ denote ReLU network classes for the pressure and flux/velocity, respectively. Thus, the network class is

$$\mathcal{N} := \mathcal{N}_p \times \mathcal{N}_u \subset \mathcal{U} \quad (4.19)$$

Note that \mathcal{U} is a convex set, while \mathcal{N} , in general, is not convex.

We now distinguish between three minimizers arising in the analysis.

- \mathbb{U}^* denotes the *global minimizer* over the ambient space \mathcal{U} , which is the unique solution of the infinite-dimensional least-squares problem. Mathematically,

$$\mathbb{U}^* := \arg \min_{\mathbb{U} \in \mathcal{U}} \Pi_{\text{LS}}[\mathbb{U}] \quad (4.20)$$

- \mathbb{U}_{dl} denotes the *continuous least-squares minimizer*, which is the minimizer of the continuous least-squares functional restricted to the network class $\mathcal{N} \subset \mathcal{U}$. Mathematically,

$$\mathbb{U}_{\text{dl}} := \arg \min_{\mathbb{U} \in \mathcal{N}} \Pi_{\text{LS}}[\mathbb{U}] \quad (4.21)$$

- In computation, Π_{LS} is replaced by a discrete (empirical) approximation Π_M , obtained for example by Monte Carlo sampling or by numerical quadrature/collocation. M is the number of collocation points where residuals and boundary mismatches are enforced. \mathbb{U}_M denotes the *trained (discrete) minimizer*, which is the minimizer of the empirical functional Π_M over \mathcal{N} . Mathematically,

$$\mathbb{U}_M := \arg \min_{\mathbb{U} \in \mathcal{N}} \Pi_M[\mathbb{U}] \quad (4.22)$$

For the convergence analysis, it is convenient to introduce the *bias gap*, which quantifies the performance loss incurred by the learned solution relative to the true optimal solution when both are evaluated under the same least-squares functional. In other words, it measures the intrinsic limitation imposed by the chosen model class. Formally, it is defined as

$$\Delta_{\mathcal{N}} := \Pi_{\text{LS}}[\mathbb{U}_{\text{dl}}] - \Pi_{\text{LS}}[\mathbb{U}^*] \quad (4.23)$$

Since \mathbb{U}^* is the global minimizer of Π_{LS} , the bias gap is necessarily non-negative, that is,

$$\Delta_{\mathcal{N}} \geq 0 \quad (4.24)$$

To study convergence toward the optimal solution, we measure the overall discrepancy between the computed solution \mathbb{U}_M and the exact minimizer \mathbb{U}^* in the norm $\|\cdot\|_{\mathcal{U}}$. The *total error* is thus defined as

$$\|\mathbb{U}_M - \mathbb{U}^*\|_{\mathcal{U}} \quad (4.25)$$

A natural starting point for the analysis is the identity

$$\mathbb{U}_M - \mathbb{U}^* = \mathbb{U}_M - \mathbb{U}_{\text{dl}} + \mathbb{U}_{\text{dl}} - \mathbb{U}^* \quad (4.26)$$

which separates the deviation into a part due to finite sampling and a part due to model approximation. Applying the triangle inequality immediately yields the error decomposition:

$$\underbrace{\|\mathbb{U}_M - \mathbb{U}^*\|_{\mathcal{U}}}_{\text{total error}} \leq \underbrace{\|\mathbb{U}_M - \mathbb{U}_{\text{dl}}\|_{\mathcal{U}}}_{\text{discretization error}} + \underbrace{\|\mathbb{U}_{\text{dl}} - \mathbb{U}^*\|_{\mathcal{U}}}_{\text{approximation error}} \quad (4.27)$$

This decomposition highlights two distinct error sources:

- (1) a *discretization (statistical) error*, stemming from the finite number of collocation points M , and
- (2) an *approximation (bias) error*, reflecting the representational limitations of the neural network class.

The goal of the convergence analysis is to show that the total error vanishes as both the network capacity (depth and width) increases and the number of collocation points M tends to infinity, thereby controlling both contributions simultaneously.

Our road map for the convergence analysis is as follows.

- (1) **Establish the mathematical target.** We analyze the continuous infinite-dimensional least-squares problem and prove existence, uniqueness, and stability of its minimizer $\mathbb{U}^* \in \mathcal{U}$. This identifies the precise solution toward which all approximations should converge.
- (2) **Quantifying approximation and discretization errors.** Building on the previously introduced DeepLS minimizers, we estimate the discrepancy caused by (i) restricting the problem to the network class (approximation/bias error) and (ii) replacing the continuous objective by its empirical counterpart (discretization error).
- (3) **Combine stability and approximation.** Using quadratic growth, we convert bounds on the functional suboptimality (i.e., $\Pi_{\text{LS}}[\mathbb{U}_M] - \Pi_{\text{LS}}[\mathbb{U}^*]$) into bounds on $\|\mathbb{U}_M - \mathbb{U}^*\|_{\mathcal{U}}$. This argument yields an explicit bound on the total error between the trained solution and the target.
- (4) **Return to the physical variables.** Finally, we transfer convergence from the transformed variables $(\mathcal{P}, \mathbf{u})$ to the physical pressure and velocity fields.

4.3. Establish the mathematical target: Continuous infinite-dimensional problem.

We now analyze the continuous problem in the infinite-dimensional setting. Our objective is to prove that it admits a unique solution and to characterize this solution both through the weak formulation and through an equivalent variational principle.

The argument proceeds in two steps. First, we establish that the bilinear form is bounded and coercive with respect to the norm $\|\cdot\|_{\mathcal{U}}$. By the Lax–Milgram theorem, these properties ensure existence and uniqueness of the solution to the associated weak formulation. Second, we show that the functional Π_{LS} is strongly convex and satisfies a quadratic-growth estimate. These properties imply that the corresponding optimization problem admits a unique minimizer. This minimizer coincides with the weak solution, thereby completing the argument.

4.3.1. *Coercivity and boundedness estimates.* We begin by establishing the coercivity of the bilinear form \mathcal{B} .

Theorem 1 (Coercivity). The bilinear form $\mathcal{B} : \mathcal{U} \times \mathcal{U} \rightarrow \mathbb{R}$ is strictly coercive on \mathcal{U} . That is, there exists $\alpha_0 > 0$ such that

$$\alpha_0 \|\mathbb{U}(\mathbf{x})\|_{\mathcal{U}}^2 \leq \mathcal{B}(\mathbb{U}(\mathbf{x}); \mathbb{U}(\mathbf{x})) \quad \forall \mathbb{U}(\mathbf{x}) \in \mathcal{U} \quad (4.28)$$

Proof. We consider the following weighted energy functional:

$$\begin{aligned} \mathcal{E}_\lambda(\mathbb{U}(\mathbf{x})) &= \lambda_1 \int_{\Omega} (\mu \mathbf{K}_0^{-1}(\mathbf{x}) \mathbf{u}(\mathbf{x}) + \text{grad}[\mathcal{P}(\mathbf{x})]) \bullet \frac{1}{\mu} \mathbf{K}_0(\mathbf{x}) (\mu \mathbf{K}_0^{-1}(\mathbf{x}) \mathbf{u}(\mathbf{x}) + \text{grad}[\mathcal{P}(\mathbf{x})]) \, d\Omega \\ &\quad + \lambda_2 \int_{\Omega} (\text{div}[\mathbf{u}(\mathbf{x})])^2 \, d\Omega + \lambda_3 \int_{\Gamma_u} (\mathbf{u}(\mathbf{x}) \bullet \hat{\mathbf{n}}(\mathbf{x}))^2 \, d\Gamma + \lambda_4 \int_{\Gamma_p} \mathcal{P}^2(\mathbf{x}) \, d\Gamma \end{aligned} \quad (4.29)$$

Expanding the first integrand and exploiting the symmetry of the tensor $\mathbf{K}_0(\mathbf{x})$, the functional can be written as

$$\begin{aligned} \mathcal{E}_\lambda(\mathbb{U}(\mathbf{x})) &= \lambda_1 \int_{\Omega} \mathbf{u}(\mathbf{x}) \bullet \mu \mathbf{K}_0^{-1}(\mathbf{x}) \mathbf{u}(\mathbf{x}) \, d\Omega + 2\lambda_1 \int_{\Omega} \mathbf{u}(\mathbf{x}) \bullet \text{grad}[\mathcal{P}(\mathbf{x})] \, d\Omega \\ &\quad + \lambda_1 \int_{\Omega} \text{grad}[\mathcal{P}(\mathbf{x})] \bullet \frac{1}{\mu} \mathbf{K}_0(\mathbf{x}) \text{grad}[\mathcal{P}(\mathbf{x})] \, d\Omega + \lambda_2 \int_{\Omega} (\text{div}[\mathbf{u}(\mathbf{x})])^2 \, d\Omega \\ &\quad + \lambda_3 \int_{\Gamma_u} (\mathbf{u}(\mathbf{x}) \bullet \hat{\mathbf{n}}(\mathbf{x}))^2 \, d\Gamma + \lambda_4 \int_{\Gamma_p} \mathcal{P}^2(\mathbf{x}) \, d\Gamma \end{aligned} \quad (4.30)$$

Using the bounds on $\mathbf{K}_0(\mathbf{x})$, we obtain the following inequality:

$$\begin{aligned} \mathcal{E}_\lambda(\mathbb{U}(\mathbf{x})) &\geq \lambda_1 \mu k_{\max}^{-1} \|\mathbf{u}(\mathbf{x})\|_{L^2(\Omega)}^2 + 2\lambda_1 \int_{\Omega} \mathbf{u}(\mathbf{x}) \bullet \text{grad}[\mathcal{P}(\mathbf{x})] \, d\Omega + \frac{\lambda_1 k_{\min}}{\mu} \|\text{grad}[\mathcal{P}(\mathbf{x})]\|_{L^2(\Omega)}^2 \\ &\quad + \lambda_2 \|\text{div}[\mathbf{u}(\mathbf{x})]\|_{L^2(\Omega)}^2 + \lambda_3 \|\mathbf{u}(\mathbf{x}) \bullet \hat{\mathbf{n}}(\mathbf{x})\|_{L^2(\Gamma_u)}^2 + \lambda_4 \|\mathcal{P}(\mathbf{x})\|_{L^2(\Gamma_p)}^2 \end{aligned} \quad (4.31)$$

By applying the Peter–Paul inequality to the second term on the right-hand side of the preceding equation, namely the mixed term, we obtain

$$\begin{aligned} \mathcal{E}_\lambda(\mathbb{U}(\mathbf{x})) &\geq \lambda_1 (\mu k_{\max}^{-1} - \varepsilon) \|\mathbf{u}(\mathbf{x})\|_{L^2(\Omega)}^2 + \lambda_1 (\mu^{-1} k_{\min} - \varepsilon^{-1}) \|\text{grad}[\mathcal{P}(\mathbf{x})]\|_{L^2(\Omega)}^2 \\ &\quad + \lambda_2 \|\text{div}[\mathbf{u}(\mathbf{x})]\|_{L^2(\Omega)}^2 + \lambda_3 \|\mathbf{u}(\mathbf{x}) \bullet \hat{\mathbf{n}}(\mathbf{x})\|_{L^2(\Gamma_u)}^2 + \lambda_4 \|\mathcal{P}(\mathbf{x})\|_{L^2(\Gamma_p)}^2 \end{aligned} \quad (4.32)$$

where $\varepsilon > 0$.

Splitting the fourth term on the right-hand side of the preceding equation (i.e., the divergence term) into two equal parts and applying the Friedrichs inequality (4.14) to one of them, we obtain

$$\begin{aligned} \mathcal{E}_\lambda(\mathbb{U}(\mathbf{x})) &\geq \left(\lambda_1 (\mu k_{\max}^{-1} - \varepsilon) + \frac{\lambda_2}{2C_{\text{div}}^2} \right) \|\mathbf{u}(\mathbf{x})\|_{L^2(\Omega)}^2 + \lambda_1 (\mu^{-1} k_{\min} - \varepsilon^{-1}) \|\text{grad}[\mathcal{P}(\mathbf{x})]\|_{L^2(\Omega)}^2 \\ &\quad + \frac{\lambda_2}{2} \|\text{div}[\mathbf{u}(\mathbf{x})]\|_{L^2(\Omega)}^2 + \left(\lambda_3 - \frac{\lambda_2}{2} \right) \|\mathbf{u}(\mathbf{x}) \bullet \widehat{\mathbf{n}}(\mathbf{x})\|_{L^2(\Gamma_u)}^2 + \lambda_4 \|\mathcal{P}(\mathbf{x})\|_{L^2(\Gamma_p)}^2 \end{aligned} \quad (4.33)$$

We now choose

$$\varepsilon = \frac{2\mu}{k_{\min}} > 0 \quad (4.34)$$

and the weights λ_i ($i = 1, \dots, 4$) as

$$\lambda_1 = 2\varepsilon = \frac{4\mu}{k_{\min}}, \quad \lambda_2 = 2C_{\text{div}}^2 \lambda_1 \varepsilon = 4C_{\text{div}}^2 \varepsilon^2 = \frac{16\mu C_{\text{div}}^2}{k_{\min}^2}, \quad \lambda_3 = \lambda_2 = \frac{16\mu C_{\text{div}}^2}{k_{\min}^2}, \quad \lambda_4 = 1 \quad (4.35)$$

With these choices, the previous estimate reduces to

$$\begin{aligned} \mathcal{E}_\lambda(\mathbb{U}(\mathbf{x})) &\geq \frac{4\mu^2}{k_{\min} k_{\max}} \|\mathbf{u}(\mathbf{x})\|_{L^2(\Omega)}^2 + 2 \|\text{grad}[\mathcal{P}(\mathbf{x})]\|_{L^2(\Omega)}^2 \\ &\quad + \frac{8\mu C_{\text{div}}^2}{k_{\min}^2} \|\text{div}[\mathbf{u}(\mathbf{x})]\|_{L^2(\Omega)}^2 + \frac{8\mu C_{\text{div}}^2}{k_{\min}^2} \|\mathbf{u}(\mathbf{x}) \bullet \widehat{\mathbf{n}}(\mathbf{x})\|_{L^2(\Gamma_u)}^2 + \|\mathcal{P}(\mathbf{x})\|_{L^2(\Gamma_p)}^2 \end{aligned} \quad (4.36)$$

Applying the Friedrichs–Poincaré inequality in squared form (4.13) to half of the second term (the one involving $\text{grad}[\mathcal{P}(\mathbf{x})]$) and absorbing the last term yields

$$\begin{aligned} \mathcal{E}_\lambda(\mathbb{U}(\mathbf{x})) &\geq \frac{4\mu^2}{k_{\min} k_{\max}} \|\mathbf{u}(\mathbf{x})\|_{L^2(\Omega)}^2 + \|\text{grad}[\mathcal{P}(\mathbf{x})]\|_{L^2(\Omega)}^2 + \frac{1}{2C_P^2} \|\mathcal{P}(\mathbf{x})\|_{L^2(\Omega)}^2 \\ &\quad + \frac{8\mu C_{\text{div}}^2}{k_{\min}^2} \|\text{div}[\mathbf{u}(\mathbf{x})]\|_{L^2(\Omega)}^2 + \frac{8\mu C_{\text{div}}^2}{k_{\min}^2} \|\mathbf{u}(\mathbf{x}) \bullet \widehat{\mathbf{n}}(\mathbf{x})\|_{L^2(\Gamma_u)}^2 \end{aligned} \quad (4.37)$$

Define

$$\Delta_1 := \min \left[\frac{4\mu^2}{k_{\min} k_{\max}}, 1, \frac{1}{2C_P^2}, \frac{8\mu C_{\text{div}}^2}{k_{\min}^2} \right] > 0 \quad (4.38)$$

Then

$$\begin{aligned} \mathcal{E}_\lambda(\mathbb{U}(\mathbf{x})) &\geq \Delta_1 \left(\|\mathcal{P}(\mathbf{x})\|_{L^2(\Omega)}^2 + \|\text{grad}[\mathcal{P}(\mathbf{x})]\|_{L^2(\Omega)}^2 + \|\mathbf{u}(\mathbf{x})\|_{L^2(\Omega)}^2 \right. \\ &\quad \left. + \|\text{div}[\mathbf{u}(\mathbf{x})]\|_{L^2(\Omega)}^2 + \|\mathbf{u}(\mathbf{x}) \bullet \widehat{\mathbf{n}}(\mathbf{x})\|_{L^2(\Gamma_u)}^2 \right) = \Delta_1 \|\mathbb{U}(\mathbf{x})\|_{\mathcal{U}}^2 \end{aligned} \quad (4.39)$$

Finally, define

$$\Delta_2 := \max [\lambda_1, \lambda_2, \lambda_3, \lambda_4] > 0 \quad (4.40)$$

It then follows that

$$\Delta_1 \|\mathbb{U}(\mathbf{x})\|_{\mathcal{U}}^2 \leq \mathcal{E}_\lambda(\mathbb{U}(\mathbf{x})) \leq \Delta_2 \mathcal{B}(\mathbb{U}(\mathbf{x}); \mathbb{U}(\mathbf{x})) \quad (4.41)$$

Choosing

$$\alpha_0 = \frac{\Delta_1}{\Delta_2} \quad (4.42)$$

yields the desired result. \square

Theorem 2 (Boundedness). The bilinear form is bounded above. That is, there exists a constant $C_B > 0$ such that

$$|\mathcal{B}(\mathbb{W}(\mathbf{x}); \mathbb{U}(\mathbf{x}))| \leq C_B \|\mathbb{W}(\mathbf{x})\|_{\mathcal{U}} \|\mathbb{U}(\mathbf{x})\|_{\mathcal{U}} \quad (4.43)$$

Proof. We decompose the bilinear form as

$$\mathcal{B}(\mathbb{W}(\mathbf{x}); \mathbb{U}(\mathbf{x})) = \mathcal{I}_1 + \mathcal{I}_2 + \mathcal{I}_3 + \mathcal{I}_4 \quad (4.44)$$

where

$$\mathcal{I}_1 := \int_{\Omega} \left(\mu \mathbf{K}_0^{-1}(\mathbf{x}) \mathbf{w}(\mathbf{x}) + \text{grad}[q(\mathbf{x})] \right) \bullet \frac{1}{\mu} \mathbf{K}_0(\mathbf{x}) \left(\mu \mathbf{K}_0^{-1}(\mathbf{x}) \mathbf{u}(\mathbf{x}) + \text{grad}[\mathcal{P}(\mathbf{x})] \right) \text{d}\Omega \quad (4.45)$$

$$\mathcal{I}_2 := \int_{\Omega} \text{div}[\mathbf{w}(\mathbf{x})] \text{div}[\mathbf{u}(\mathbf{x})] \text{d}\Omega \quad (4.46)$$

$$\mathcal{I}_3 := \int_{\Gamma_u} (\mathbf{w}(\mathbf{x}) \bullet \hat{\mathbf{n}}(\mathbf{x})) (\mathbf{u}(\mathbf{x}) \bullet \hat{\mathbf{n}}(\mathbf{x})) \text{d}\Gamma \quad (4.47)$$

$$\mathcal{I}_4 := \int_{\Gamma_p} q(\mathbf{x}) \mathcal{P}(\mathbf{x}) \text{d}\Gamma \quad (4.48)$$

Estimating \mathcal{I}_1 . Using the Cauchy–Schwarz inequality and invoking the bounds on $\mathbf{K}_0(\mathbf{x})$, we proceed as follows:

$$\begin{aligned} |\mathcal{I}_1| &\leq \left\| \mu \mathbf{K}_0^{-1}(\mathbf{x}) \mathbf{w}(\mathbf{x}) + \text{grad}[q(\mathbf{x})] \right\|_{L^2(\Omega)} \left\| \frac{1}{\mu} \mathbf{K}_0(\mathbf{x}) (\mu \mathbf{K}_0^{-1}(\mathbf{x}) \mathbf{u}(\mathbf{x}) + \text{grad}[\mathcal{P}(\mathbf{x})]) \right\|_{L^2(\Omega)} \\ &\leq \frac{k_{\max}}{\mu} \left\| \mu \mathbf{K}_0^{-1}(\mathbf{x}) \mathbf{w}(\mathbf{x}) + \text{grad}[q(\mathbf{x})] \right\|_{L^2(\Omega)} \left\| \mu \mathbf{K}_0^{-1}(\mathbf{x}) \mathbf{u}(\mathbf{x}) + \text{grad}[\mathcal{P}(\mathbf{x})] \right\|_{L^2(\Omega)} \\ &\leq \frac{k_{\max}}{\mu} \left(\mu k_{\min}^{-1}(\mathbf{x}) \|\mathbf{w}(\mathbf{x})\|_{L^2(\Omega)} + \|\text{grad}[q(\mathbf{x})]\|_{L^2(\Omega)} \right) \left(\mu k_{\min}^{-1}(\mathbf{x}) \|\mathbf{u}(\mathbf{x})\|_{L^2(\Omega)} + \|\text{grad}[\mathcal{P}(\mathbf{x})]\|_{L^2(\Omega)} \right) \\ &\leq C_1 \left(\|\mathbf{w}(\mathbf{x})\|_{L^2(\Omega)} + \|\text{grad}[q(\mathbf{x})]\|_{L^2(\Omega)} \right) \left(\|\mathbf{u}(\mathbf{x})\|_{L^2(\Omega)} + \|\text{grad}[\mathcal{P}(\mathbf{x})]\|_{L^2(\Omega)} \right) \end{aligned} \quad (4.49)$$

where

$$C_1 := \frac{k_{\max}}{\mu} (\mu k_{\min}^{-1} + 1)^2 \quad (4.50)$$

The continuous embeddings of the underlying function spaces imply the following norm inequalities:

$$\|\mathbf{v}(\mathbf{x})\|_{L^2(\Omega)} \leq \|\mathbf{v}(\mathbf{x})\|_{H(\text{div}; \Omega)} \leq \|\mathbf{v}(\mathbf{x})\|_{H(\text{div}; \Omega, \Gamma_u)} \quad \text{and} \quad \|\text{grad}[r(\mathbf{x})]\|_{L^2(\Omega)} \leq \|r(\mathbf{x})\|_{H^1(\Omega)} \quad (4.51)$$

These estimates enable us to derive the following inequality from Eq. (4.49):

$$|\mathcal{I}_1| \leq C_1 \|\mathbb{W}(\mathbf{x})\|_{\mathcal{U}} \|\mathbb{U}(\mathbf{x})\|_{\mathcal{U}} \quad (4.52)$$

Estimating \mathcal{I}_2 . Using the Cauchy–Schwarz inequality, we write

$$|\mathcal{I}_2| \leq \|\text{div}[\mathbf{w}]\|_{L^2(\Omega)} \|\text{div}[\mathbf{u}]\|_{L^2(\Omega)} \leq \|\mathbf{w}\|_{H(\text{div}; \Omega)} \|\mathbf{u}\|_{H(\text{div}; \Omega)} \leq \|\mathbb{W}\|_{\mathcal{U}} \|\mathbb{U}\|_{\mathcal{U}} \quad (4.53)$$

Estimating \mathcal{I}_3 . Again using the Cauchy–Schwarz inequality on Γ_u , we establish

$$|\mathcal{I}_3| \leq \|\mathbf{w}(\mathbf{x}) \bullet \hat{\mathbf{n}}(\mathbf{x})\|_{L^2(\Gamma_u)} \|\mathbf{u}(\mathbf{x}) \bullet \hat{\mathbf{n}}(\mathbf{x})\|_{L^2(\Gamma_u)} \leq \|\mathbb{W}(\mathbf{x})\|_{\mathcal{U}} \|\mathbb{U}(\mathbf{x})\|_{\mathcal{U}} \quad (4.54)$$

Estimating \mathcal{I}_4 . By the Cauchy–Schwarz inequality and the trace inequality (4.11), we write

$$|\mathcal{I}_4| \leq \|q\|_{L^2(\Gamma_p)} \|\mathcal{P}\|_{L^2(\Gamma_p)} \leq C_{\text{tr}}^2 \|q\|_{H^1(\Omega)} \|\mathcal{P}\|_{H^1(\Omega)} \leq C_{\text{tr}}^2 \|\mathbb{W}\|_{\mathcal{U}} \|\mathbb{U}\|_{\mathcal{U}} \quad (4.55)$$

Collecting the above estimates yields

$$|\mathcal{B}(\mathbb{W}(\mathbf{x}); \mathbb{U}(\mathbf{x}))| \leq C_B \|\mathbb{W}(\mathbf{x})\|_{\mathcal{U}} \|\mathbb{U}(\mathbf{x})\|_{\mathcal{U}} \quad (4.56)$$

with

$$C_B := C_1 + 2 + C_{\text{tr}}^2 \quad (4.57)$$

This proves that the bilinear form $\mathcal{B}(\cdot; \cdot)$ is bounded on $\mathcal{U} \times \mathcal{U}$. \square

Since the bilinear form $\mathcal{B}(\cdot, \cdot)$ is coercive and continuous on \mathcal{U} , the Lax–Milgram theorem [Brezis, 2011] guarantees that the weak problem (4.15) admits a unique solution $\mathbb{U}(\mathbf{x}) \in \mathcal{U}$. Moreover, the solution depends continuously on the data; in particular, there exists a constant $C > 0$ such that

$$\|\mathbb{U}(\mathbf{x})\|_{\mathcal{U}} \leq C \|\ell\|_{\mathcal{U}^*} \quad (4.58)$$

Here, \mathcal{U}^* denotes the dual space of \mathcal{U} and $\|\cdot\|_{\mathcal{U}^*}$ is the associated dual norm.

4.3.2. Strong convexity and quadratic growth. Building on the coercivity established above, we now prove that the functional Π_{LS} is strongly convex and derive the associated quadratic-growth estimate.

Lemma 3 (Strong convexity of Π_{LS}). Π_{LS} is α_0 -strongly convex on \mathcal{U} . That is, for all $\mathbb{U}, \mathbb{V} \in \mathcal{U}$ and all $\theta \in [0, 1]$, we have

$$\Pi_{\text{LS}}[\theta \mathbb{U} + (1 - \theta) \mathbb{V}] \leq \theta \Pi_{\text{LS}}[\mathbb{U}] + (1 - \theta) \Pi_{\text{LS}}[\mathbb{V}] - \frac{\alpha_0}{2} \theta(1 - \theta) \|\mathbb{U} - \mathbb{V}\|_{\mathcal{U}}^2 \quad (4.59)$$

Proof. The α_0 -strong convexity is a direct consequence symmetry, bilinearity, and coercivity of $\mathcal{B}(\cdot; \cdot)$. To wit, for $\mathbb{U}, \mathbb{V} \in \mathcal{U}$ and $\theta \in [0, 1]$ we have

$$\theta \Pi_{\text{LS}}[\mathbb{U}] + (1 - \theta) \Pi_{\text{LS}}[\mathbb{V}] - \Pi_{\text{LS}}[\theta \mathbb{U} + (1 - \theta) \mathbb{V}] = \frac{1}{2} \theta(1 - \theta) \mathcal{B}(\mathbb{U} - \mathbb{V}; \mathbb{U} - \mathbb{V}) \quad (4.60)$$

By coercivity (see Theorem (1)), we write

$$\frac{1}{2} \theta(1 - \theta) \mathcal{B}(\mathbb{U} - \mathbb{V}; \mathbb{U} - \mathbb{V}) \geq \frac{\alpha_0}{2} \theta(1 - \theta) \|\mathbb{U} - \mathbb{V}\|_{\mathcal{U}}^2 \quad (4.61)$$

which is equivalent to (4.59). \square

Lemma 4 (Unique global minimizer \mathbb{U}^*). Π_{LS} has a unique minimizer $\mathbb{U}^* \in \mathcal{U}$.

Proof. Suppose that \mathbb{U}_1^* and \mathbb{U}_2^* are two distinct minimizers. Applying the strong convexity estimate (4.59) with $\theta = \frac{1}{2}$, $\mathbb{U} = \mathbb{U}_1^*$, $\mathbb{V} = \mathbb{U}_2^*$ gives

$$\Pi_{\text{LS}}\left[\frac{1}{2}(\mathbb{U}_1^* + \mathbb{U}_2^*)\right] \leq \frac{1}{2}\Pi_{\text{LS}}[\mathbb{U}_1^*] + \frac{1}{2}\Pi_{\text{LS}}[\mathbb{U}_2^*] - \frac{\alpha_0}{8} \|\mathbb{U}_1^* - \mathbb{U}_2^*\|_{\mathcal{U}}^2 \quad (4.62)$$

Because both \mathbb{U}_1^* and \mathbb{U}_2^* are minimizers, they have the same minimal value:

$$\Pi_{\text{LS}}[\mathbb{U}_1^*] = \Pi_{\text{LS}}[\mathbb{U}_2^*] \quad (4.63)$$

Hence, we have

$$\Pi_{\text{LS}}[\bar{\mathbb{U}}] \leq \Pi_{\text{LS}}[\mathbb{U}_1^*] - \frac{\alpha_0}{8} \|\mathbb{U}_1^* - \mathbb{U}_2^*\|_{\mathcal{U}}^2 \quad (4.64)$$

If $\mathbb{U}_1^* \neq \mathbb{U}_2^*$, then $\|\mathbb{U}_1^* - \mathbb{U}_2^*\|_{\mathcal{U}}^2 > 0$, and the right-hand side is strictly smaller than $\Pi_{\text{LS}}(\mathbb{U}_1^*)$. This contradicts the minimality of \mathbb{U}_1^* . Therefore,

$$\|\mathbb{U}_1^* - \mathbb{U}_2^*\|_{\mathcal{U}}^2 = 0 \quad (4.65)$$

which further implies $\mathbb{U}_1^* = \mathbb{U}_2^*$. \square

Lemma 5 (Quadratic growth (QG) of Π_{LS}). The functional Π_{LS} satisfies the quadratic-growth estimate about its global minimizer $\mathbb{U}^* \in \mathcal{U}$:

$$\Pi_{\text{LS}}[\mathbb{U}] - \Pi_{\text{LS}}[\mathbb{U}^*] \geq \frac{\alpha_0}{2} \|\mathbb{U} - \mathbb{U}^*\|_{\mathcal{U}}^2, \quad \forall \mathbb{U} \in \mathcal{U} \quad (4.66)$$

Proof. Let $\mathbb{U}^* \in \mathcal{U}$ be a minimizer of Π_{LS} over \mathcal{U} . Fix any $\mathbb{U} \in \mathcal{U}$ and $\theta \in (0, 1)$. Applying (4.59) with $\mathbb{V} = \mathbb{U}^*$ yields

$$\Pi_{\text{LS}}[\theta\mathbb{U} + (1 - \theta)\mathbb{U}^*] \leq \theta\Pi_{\text{LS}}[\mathbb{U}] + (1 - \theta)\Pi_{\text{LS}}[\mathbb{U}^*] - \frac{\alpha_0}{2}\theta(1 - \theta)\|\mathbb{U} - \mathbb{U}^*\|_{\mathcal{U}}^2 \quad (4.67)$$

Since \mathcal{U} is convex, $\theta\mathbb{U} + (1 - \theta)\mathbb{U}^* \in \mathcal{U}$, and by optimality of \mathbb{U}^* we have

$$\Pi_{\text{LS}}[\mathbb{U}^*] \leq \Pi_{\text{LS}}[\theta\mathbb{U} + (1 - \theta)\mathbb{U}^*] \quad (4.68)$$

Combining the two inequalities gives

$$\Pi_{\text{LS}}[\mathbb{U}^*] \leq \theta\Pi_{\text{LS}}[\mathbb{U}] + (1 - \theta)\Pi_{\text{LS}}[\mathbb{U}^*] - \frac{\alpha_0}{2}\theta(1 - \theta)\|\mathbb{U} - \mathbb{U}^*\|_{\mathcal{U}}^2 \quad (4.69)$$

Rearranging and dividing by $\theta > 0$ yields

$$\Pi_{\text{LS}}[\mathbb{U}] - \Pi_{\text{LS}}[\mathbb{U}^*] \geq \frac{\alpha_0}{2}(1 - \theta)\|\mathbb{U} - \mathbb{U}^*\|_{\mathcal{U}}^2 \quad (4.70)$$

Letting $\theta \downarrow 0$ gives the quadratic-growth estimate

$$\Pi_{\text{LS}}[\mathbb{U}] - \Pi_{\text{LS}}[\mathbb{U}^*] \geq \frac{\alpha_0}{2} \|\mathbb{U} - \mathbb{U}^*\|_{\mathcal{U}}^2, \quad \forall \mathbb{U} \in \mathcal{U} \quad (4.71)$$

\square

4.4. Quantifying approximation and discretization errors. Having established well-posedness and stability of the continuous least-squares problem, we now quantify the two mechanisms that separate the trained DeepLS solution from the target solution \mathbb{U}^* . The first source of error arises from restricting the optimization problem to the neural network class \mathcal{N} , leading to an approximation (bias) error. The second source stems from replacing the continuous least-squares functional Π_{LS} by its empirical counterpart Π_M , leading to a discretization (or statistical) error. In this subsection, we estimate each contribution separately at the level of the objective functional. These bounds will later be combined with the quadratic-growth property to obtain convergence in the \mathcal{U} norm.

The comparison between the continuous and discrete minimizers relies on controlling the discrepancy between the continuous least-squares functional Π_{LS} and its empirical approximation Π_M . In particular, we require a uniform bound on this discrepancy over the network class \mathcal{N} . Such a bound ensures that the discrete objective provides a reliable approximation of the continuous one and forms the key ingredient in relating the trained network solution to the continuous deep least-squares minimizer.

Lemma 6 (Uniform perturbation (UP) bound on network class \mathcal{N}). For every $\delta \in (0, 1)$ there exists $\varepsilon_{\text{disc}}(M, \delta)$ with $\varepsilon_{\text{disc}}(M, \delta) \rightarrow 0$ as $M \rightarrow \infty$ such that

$$\sup_{(\mathcal{P}, \mathbf{u}) \in \mathcal{N}} \left| \Pi_{\text{LS}}[\mathcal{P}, \mathbf{u}] - \Pi_M[\mathcal{P}, \mathbf{u}] \right| \leq \varepsilon_{\text{disc}}(M, \delta) \quad (4.72)$$

with probability at least $1 - \delta$.

Proof. This is a standard uniform law of large numbers (uniform deviation) result for the empirical objective Π_M over the hypothesis class $\mathcal{N}_p \times \mathcal{N}_u$; see [van der Vaart and Wellner \[1996, Chs. 2–3\]](#). In the sample-average approximation (SAA) viewpoint, the same uniform perturbation bound follows from the basic stability theory of stochastic programming; see [Shapiro et al. \[2014, Ch. 3\]](#). \square

Remark 5 (Deterministic discretization error). If the discrete functional Π_M is obtained from a *deterministic* discretization of Π_{LS} (e.g., a fixed quadrature rule such as Gaussian quadrature or sparse grids, mesh-based collocation with deterministic points, or deterministic cubature rules with proven error estimates), then Π_M is non-random and the functional perturbation estimate can be stated *without* probability. In this case, one assumes the deterministic bound

$$\sup_{(\mathcal{P}, \mathbf{u}) \in \mathcal{N}} \left| \Pi_{\text{LS}}[\mathcal{P}(\mathbf{x}), \mathbf{u}(\mathbf{x})] - \Pi_M[\mathcal{P}(\mathbf{x}), \mathbf{u}(\mathbf{x})] \right| \leq \varepsilon_{\text{disc}}(M) \quad (4.73)$$

where $\varepsilon_{\text{disc}}(M)$ is a quadrature/cubature (or collocation) consistency error estimate, often expressed equivalently in terms of a mesh size h rather than the number of quadrature/collocation points M .

Theorem 7 (Existence of a network approximant in \mathcal{U}). Let $\Omega \subset \mathbb{R}^{nd}$ be a bounded Lipschitz domain. Then ReLU network pairs are dense in \mathcal{U} . More precisely, for every $\varepsilon > 0$ there exists a network pair

$$\tilde{\mathbb{U}} = (\tilde{\mathcal{P}}, \tilde{\mathbf{u}}) \in \mathcal{N}(\text{depth}, \text{width}) \quad (4.74)$$

with depth and width chosen sufficiently large (depending on ε and nd) such that

$$\|\tilde{\mathbb{U}} - \mathbb{U}^*\|_{\mathcal{U}} \leq \varepsilon \quad (4.75)$$

Equivalently, defining the best-approximation error

$$\varepsilon_{\text{app}}(\text{depth}, \text{width}) := \inf_{\mathbb{U} \in \mathcal{N}(\text{depth}, \text{width})} \|\mathbb{U} - \mathbb{U}^*\|_{\mathcal{U}} \quad (4.76)$$

one has

$$\varepsilon_{\text{app}}(\text{depth}, \text{width}) \rightarrow 0 \quad (4.77)$$

as the architecture is enriched.

Proof. The claim is a direct application of Sobolev-approximation results for deep ReLU networks. Concretely, the approximation theorem of [Gühring et al. \[2020, Theorem 4.1\]](#) shows that for bounded Lipschitz domains $\Omega \subset \mathbb{R}^{nd}$ and for target functions in the relevant Sobolev class, ReLU networks are dense in the corresponding Sobolev norm, with an explicit depth/width (or nonzero-weight) requirement depending on the dimension nd and the tolerance.

Apply this result componentwise to \mathcal{P}^* and to each component of \mathbf{u}^* , and combine the componentwise estimates using the definition of the product norm $\|\cdot\|_{\mathcal{U}}$ to obtain: for every $\varepsilon > 0$ there exist depths/widths large enough and a network pair $\tilde{\mathbb{U}} \in \mathcal{N}(\text{depth}, \text{width})$ such that inequality (4.75) holds.

Finally, the definition (4.76) immediately implies that $\varepsilon_{\text{app}}(\text{depth}, \text{width})$ is nonincreasing under architecture enrichment and tends to 0 along any sequence of architectures for which the above density statement is enforced. The last inequality (4.77) follows from the definition of an infimum. \square

Remark 6. Although the proof of Theorem 7 considered ReLU activation function, it did not use any special structural property of the ReLU activation beyond the availability of a Sobolev density result for the corresponding network class. The argument only requires that the network class be dense in the Sobolev spaces underlying the $\|\cdot\|_{\mathcal{U}}$ -norm—in particular, dense in $H^1(\Omega)$ for the pressure component and component-wise dense in a Sobolev space ensuring that the divergence and trace terms in $\|\cdot\|_{\mathcal{U}}$ are well-defined. Hence, the same conclusion holds for any activation function σ such that \mathcal{N}_σ enjoys the corresponding Sobolev density property. In particular:

- For piecewise-linear two-slope activations (e.g., leaky-ReLU, PReLU), ReLU can be expressed as an affine combination of σ and the identity, so any ReLU network can be rewritten as a σ -network up to a constant-factor change in parameters. The ReLU-based density result therefore applies directly.
- For smooth non-polynomial activations (e.g., tanh, sigmoid, softplus), Sobolev-norm approximation theorems are available (see, e.g., [Ryck et al., 2021; Siegel and Xu, 2020]), yielding the same existence result, possibly with different architectural requirements and approximation rates.

Theorem 8 (Bias gap bound). The bias gap satisfies

$$\Delta_{\mathcal{N}} \leq \frac{C_{\mathcal{B}}}{2} \left(\varepsilon_{\text{app}}(\text{depth}, \text{width}) \right)^2 \quad (4.78)$$

In particular, if $\varepsilon_{\text{app}}(\text{depth}, \text{width}) \rightarrow 0$ as the architecture is enriched, then $\Delta_{\mathcal{N}} \rightarrow 0$.

Proof. Let $\mathbb{U}_{\text{dl}} \in \mathcal{N}$ be a minimizer of Π_{LS} over \mathcal{N} , and let $\tilde{\mathbb{U}} \in \mathcal{N}$ be arbitrary. By minimality of \mathbb{U}_{dl} on \mathcal{N} , we write

$$\Delta_{\mathcal{N}} = \Pi_{\text{LS}}[\mathbb{U}_{\text{dl}}] - \Pi_{\text{LS}}[\mathbb{U}^*] \leq \Pi_{\text{LS}}[\tilde{\mathbb{U}}] - \Pi_{\text{LS}}[\mathbb{U}^*] \quad (4.79)$$

Step 1: Energy identity. Recall that the least-squares functional has the quadratic form

$$\Pi_{\text{LS}}[\mathbb{U}] = \frac{1}{2} \mathcal{B}(\mathbb{U}; \mathbb{U}) - \ell(\mathbb{U}) \quad (4.80)$$

Moreover, $\mathbb{U}^* \in \mathcal{U}$ is the unique solution of the associated normal equations

$$\mathcal{B}(\mathbb{U}^*; \mathbb{V}) = \ell(\mathbb{V}) \quad \forall \mathbb{V} \in \mathcal{U} \quad (4.81)$$

Set $\mathbb{E} := \mathbb{U} - \mathbb{U}^*$. Expanding Eq. (4.80) at \mathbb{U}^* yields

$$\begin{aligned} \Pi_{\text{LS}}[\mathbb{U}] - \Pi_{\text{LS}}[\mathbb{U}^*] &= \frac{1}{2} \left(\mathcal{B}(\mathbb{U}^* + \mathbb{E}; \mathbb{U}^* + \mathbb{E}) - \mathcal{B}(\mathbb{U}^*; \mathbb{U}^*) \right) - (\ell(\mathbb{U}^* + \mathbb{E}) - \ell(\mathbb{U}^*)) \\ &= \frac{1}{2} \left(2 \mathcal{B}(\mathbb{U}^*; \mathbb{E}) + \mathcal{B}(\mathbb{E}; \mathbb{E}) \right) - \ell(\mathbb{E}) \\ &= \mathcal{B}(\mathbb{U}^*; \mathbb{E}) - \ell(\mathbb{E}) + \frac{1}{2} \mathcal{B}(\mathbb{E}; \mathbb{E}) \end{aligned} \quad (4.82)$$

Using Eq. (4.81) with $\mathbb{V} = \mathbb{E}$ gives $\ell(\mathbb{E}) = \mathcal{B}(\mathbb{U}^*; \mathbb{E})$; hence, the cross term cancels, and we obtain the *energy identity*:

$$\Pi_{\text{LS}}[\mathbb{U}] - \Pi_{\text{LS}}[\mathbb{U}^*] = \frac{1}{2} \mathcal{B}(\mathbb{U} - \mathbb{U}^*; \mathbb{U} - \mathbb{U}^*) \quad \text{for all } \mathbb{U} \in \mathcal{U} \quad (4.83)$$

Step 2: Apply the energy identity and bound. Applying (4.83) with $\mathbb{U} = \tilde{\mathbb{U}}$ and then using the boundedness of the bilinear form (i.e., Theorem 2) yields

$$\Pi_{\text{LS}}[\tilde{\mathbb{U}}] - \Pi_{\text{LS}}[\mathbb{U}^*] = \frac{1}{2} \mathcal{B}(\tilde{\mathbb{U}} - \mathbb{U}^*; \tilde{\mathbb{U}} - \mathbb{U}^*) \leq \frac{C_{\mathcal{B}}}{2} \|\tilde{\mathbb{U}} - \mathbb{U}^*\|_{\mathcal{U}}^2 \quad (4.84)$$

Step 3: Insert the network approximation bound. By Theorem 7, there exists $\tilde{\mathbb{U}} \in \mathcal{N}$ such that

$$\|\tilde{\mathbb{U}} - \mathbb{U}^*\|_{\mathcal{U}} \leq \varepsilon_{\text{app}}(\text{depth}, \text{width}) \quad (4.85)$$

Combining this with Eqs. (4.79)–(4.84) gives

$$\Delta_{\mathcal{N}} \leq \frac{C_{\mathcal{B}}}{2} \left(\varepsilon_{\text{app}}(\text{depth}, \text{width}) \right)^2 \quad (4.86)$$

which is exactly Eq. (4.78). The final statement follows immediately. \square

4.5. Combine stability and approximation. We now combine the stability of the continuous problem with the approximation and discretization estimates derived above. The quadratic-growth property of Π_{LS} converts objective-level bounds into norm bounds in \mathcal{U} , yielding an explicit total-error estimate and convergence of the trained solution.

Theorem 9 (Estimating the total error in the transformed variables). The discrete minimizer \mathbb{U}_M and the global minimizer \mathbb{U}^* satisfy

$$\|\mathbb{U}_M - \mathbb{U}^*\|_{\mathcal{U}} \leq \sqrt{\frac{2}{\alpha_0} \left(\Delta_{\mathcal{N}} + 2\varepsilon_{\text{disc}}(M, \delta) \right)} \quad (4.87)$$

where

$$\Delta_{\mathcal{N}} := \Pi_{\text{LS}}[\mathbb{U}_{\text{dl}}] - \Pi_{\text{LS}}[\mathbb{U}^*] \geq 0$$

In particular, if $\Delta_{\mathcal{N}} \rightarrow 0$ (e.g., by a depth/width approximation theorem as the network class is enriched) and $\varepsilon_{\text{disc}}(M, \delta) \rightarrow 0$ as $M \rightarrow \infty$, then $\mathbb{U}_M \rightarrow \mathbb{U}^*$ in $\|\cdot\|_{\mathcal{U}}$.

Proof. By the uniform perturbation bound (given by Lemma 6), for every $(\mathcal{P}, \mathbf{u}) \in \mathcal{N}$, we have

$$|\Pi_{\text{LS}}[\mathcal{P}, \mathbf{u}] - \Pi_M[\mathcal{P}, \mathbf{u}]| \leq \varepsilon_{\text{disc}}(M, \delta) \quad (4.88)$$

In particular,

$$\Pi_{\text{LS}}[\mathcal{P}, \mathbf{u}] \leq \Pi_M[\mathcal{P}, \mathbf{u}] + \varepsilon_{\text{disc}}(M, \delta) \quad \text{and} \quad \Pi_M[\mathcal{P}, \mathbf{u}] \leq \Pi_{\text{LS}}[\mathcal{P}, \mathbf{u}] + \varepsilon_{\text{disc}}(M, \delta) \quad \text{on } \mathcal{N} \quad (4.89)$$

Since \mathbb{U}_M minimizes Π_M over \mathcal{N} , we establish

$$\Pi_M[\mathbb{U}_M] \leq \Pi_M[\mathbb{U}_{\text{dl}}] \quad (4.90)$$

Hence, we write

$$\Pi_{\text{LS}}(\mathbb{U}_M) \leq \Pi_M[\mathbb{U}_M] + \varepsilon_{\text{disc}} \leq \Pi_M[\mathbb{U}_{\text{dl}}] + \varepsilon_{\text{disc}} \leq \Pi_{\text{LS}}[\mathbb{U}_{\text{dl}}] + 2\varepsilon_{\text{disc}} \quad (4.91)$$

Subtracting $\Pi_{\text{LS}}[\mathbb{U}^*]$ and using the definition of $\Delta_{\mathcal{N}}$ gives

$$\Pi_{\text{LS}}[\mathbb{U}_M] - \Pi_{\text{LS}}[\mathbb{U}^*] \leq \Delta_{\mathcal{N}} + 2\varepsilon_{\text{disc}} \quad (4.92)$$

Applying quadratic growth on \mathcal{U} with $\mathbb{U} = \mathbb{U}_M$ yields

$$\frac{\alpha_0}{2} \|\mathbb{U}_M - \mathbb{U}^*\|_{\mathcal{U}}^2 \leq \Pi_{\text{LS}}[\mathbb{U}_M] - \Pi_{\text{LS}}[\mathbb{U}^*] \leq \Delta_{\mathcal{N}} + 2\varepsilon_{\text{disc}}(M, \delta) \quad (4.93)$$

which proves the claim after rearranging and taking square roots. \square

4.6. Convergence in physical variables. Since $\mathcal{U}_M = (\mathcal{P}_M, \mathbf{u}_M)$ converges to $\mathcal{U}^* = (\mathcal{P}^*, \mathbf{u}^*)$ in \mathcal{U} , and since the Lambert–W transformation mapping the transformed variable $\mathcal{P}(\mathbf{x})$ to the physical pressure $p(\mathbf{x})$ is continuous, convergence is preserved under this transformation. Hence, the reconstructed physical pressure field obtained from \mathcal{P}_M converges to the exact physical pressure corresponding to \mathcal{P}^* .

Moreover, the velocity field is unaffected by the Hopf–Cole transformation, as the transformation acts solely on the pressure variable. The velocity $\mathbf{u}(\mathbf{x})$ is represented directly in the DeepLS formulation and therefore does not undergo any nonlinear mapping. Consequently, convergence of \mathbf{u}_M to \mathbf{u}^* immediately implies convergence of the physical velocity field.

In summary, the solution produced by the DeepLS framework—combining the Hopf–Cole transformation with deep neural networks within a least-squares formulation—converges to the exact solution field of the nonlinear Klinkenberg model in both pressure and velocity variables. This finishes the convergence analysis.

5. REPRESENTATION NUMERICAL RESULTS

We present numerical results for several canonical problems to:

- (1) Establish the accuracy of the proposed framework through comparisons with analytical solutions where available and with finite element solutions otherwise.
- (2) Demonstrate numerical convergence under systematic refinements in network width and depth.
- (3) Quantify time-to-solution performance.

5.1. Gas flow through concentric cylinders. Solving this boundary-value problem serves several purposes. Physically, gas flow in an annular porous domain occurs in subsurface and laboratory settings such as radial flow around wells, core-scale permeability measurements, and pneumatic testing of low-permeability media, where rarefaction effects may be significant [Wu et al., 1998]. From a modeling standpoint, the configuration provides a canonical axisymmetric benchmark for evaluating the DeepLS framework’s ability to resolve radial flow. Specifically, the analysis (i) validates DeepLS against closed-form analytical pressure and velocity solutions and (ii) isolates the impact of the Klinkenberg correction by comparison with the classical Darcy model under identical boundary conditions.

We consider gas flow in an annular porous domain bounded by two concentric circles of inner radius r_i and outer radius r_o . Prescribed pressures are imposed on the inner and outer boundaries, as illustrated in **Fig. 3**. Owing to the rotational symmetry of the geometry and boundary data, the solution is axisymmetric: the pressure and velocity only depend on the radial coordinate r . The corresponding analytical expressions for these fields are given by:

$$p(r) = \beta p_{\text{atm}} W\left(\frac{1}{\beta p_{\text{atm}}} \exp\left(\frac{\mathcal{P}(r)}{\beta p_{\text{atm}}}\right)\right) \quad (5.1)$$

$$v_r(r) = \frac{K_0}{\mu} \frac{(p_i - p_o) + \beta p_{\text{atm}} (\ln(p_i) - \ln(p_o))}{\ln(r_o) - \ln(r_i)} \frac{1}{r} \quad (5.2)$$

where the transformed pressure field is

$$\mathcal{P}(r) = \mathcal{P}_i + (\mathcal{P}_o - \mathcal{P}_i) \left(\frac{\ln(r) - \ln(r_i)}{\ln(r_o) - \ln(r_i)} \right) \quad r_i < r < r_o \quad (5.3)$$

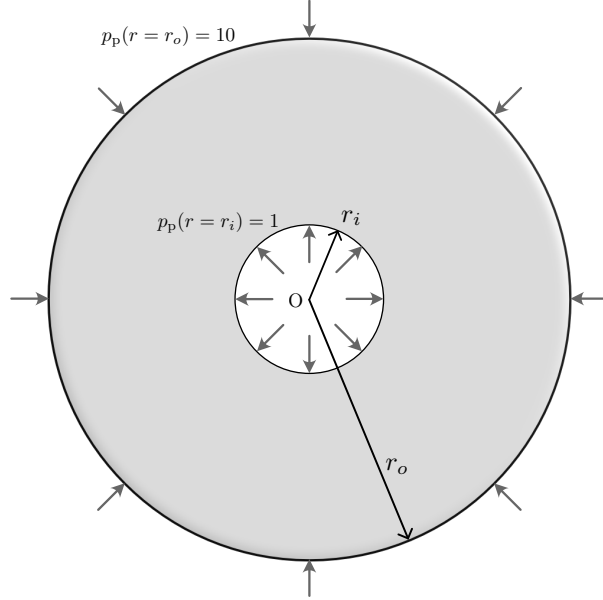


Figure 3. Gas flow through concentric cylinders. Schematic of a pressure-driven gas flow problem in an annular porous domain bounded by two concentric circles with radii r_i and r_o . Prescribed pressures at the inner ($p_p(r_i) = 10$) and outer ($p_p(r_o) = 1$) boundaries induce an axisymmetric pressure field and the corresponding radial flow.

The material parameters and geometric details used in the simulation are summarized in Table 2. The problem is solved using the proposed DeepLS framework, and the resulting pressure and velocity fields are shown in Fig. 4. The numerical results are in excellent agreement with the analytical solution, as illustrated in Fig. 5. These results were obtained using a neural network with six hidden layers and 64 neurons per layer, trained with the ReLU activation function; the total training time on an NVIDIA T4 GPU was 6.34 minutes.

Table 2. Gas flow through concentric cylinders. Material and geometry parameters.

| Parameter | Value |
|---------------------------------|----------------------|
| β | 1 |
| μ | 1 |
| $\gamma \mathbf{b}(\mathbf{x})$ | $\approx \mathbf{0}$ |
| k_0 | 1 |
| r_i | 0.3 |
| r_o | 1.0 |

5.1.1. *Influence of network depth and width on accuracy.* To examine how the approximation accuracy of the proposed DeepLS framework depends on the neural network architecture, we conduct a controlled capacity study in which the network depth and width are systematically varied. Let L denote the *depth* (i.e., the number of hidden layers) and m the *width* (i.e., the number of neurons per hidden layer). The discrepancy between the neural approximation, denoted by \hat{u}_θ , and

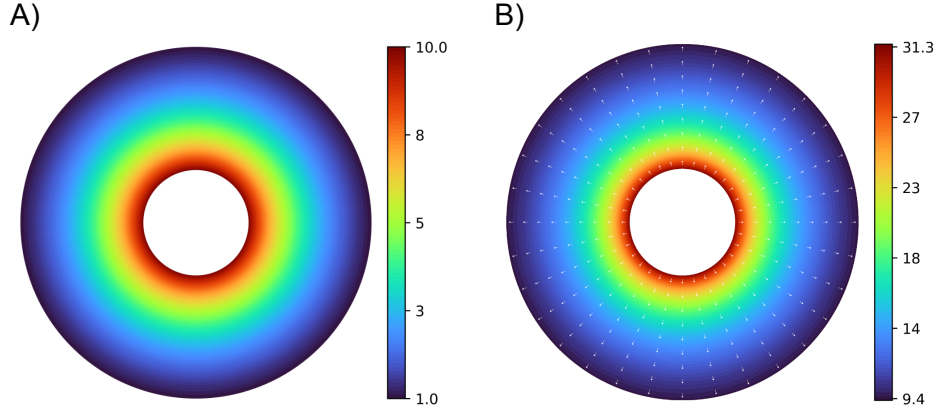


Figure 4. Gas flow through concentric cylinders. (A) Contours of the pressure field $p(\mathbf{x})$ in the concentric annular domain obtained with the proposed DeepLS framework under the Klinkenberg model, showing radial decay from the inner to the outer boundary. (B) Contours of the corresponding velocity magnitude $\|\mathbf{u}(\mathbf{x})\|$, with superimposed velocity vectors indicating a purely radial flow, attaining a maximum near the inner boundary and decreasing monotonically toward the outer boundary.

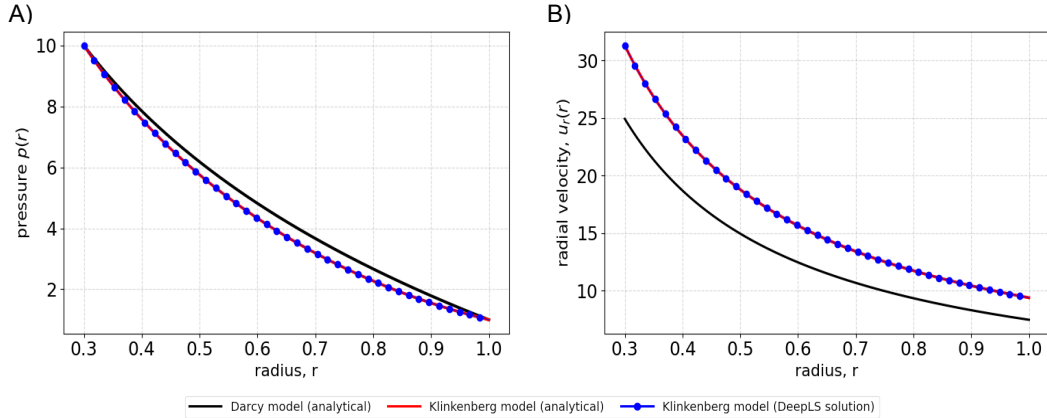


Figure 5. Gas flow through concentric cylinders. Analytical and DeepLS solution fields for the concentric-cylinder benchmark, comparing the classical Darcy model with the pressure-dependent Klinkenberg formulation. (A) Radial pressure profile as a function of radius: Darcy (constant permeability), analytical Klinkenberg solution obtained via the Hopf-Cole transformation, and the DeepLS prediction. (B) Radial velocity profile showing agreement between DeepLS and the analytical Klinkenberg solution, and deviation from the classical Darcy response due to slip-induced permeability enhancement.

a reference solution u_{ref} (analytical) is quantified using the $L_2(\Omega)$ error:

$$\|\widehat{u}_\theta - u_{\text{ref}}\|_{L_2(\Omega)} := \left(\int_{\Omega} (\widehat{u}_\theta(\mathbf{x}) - u_{\text{ref}}(\mathbf{x}))^2 d\Omega \right)^{1/2} \quad (5.4)$$

Figure 6A shows the error as a function of a global capacity measure, the total number of neurons N_{tot} , used as a proxy for the size of the parametric trial space. Two regimes are evident. At low capacity, the error remains relatively large and decreases slowly, indicating an

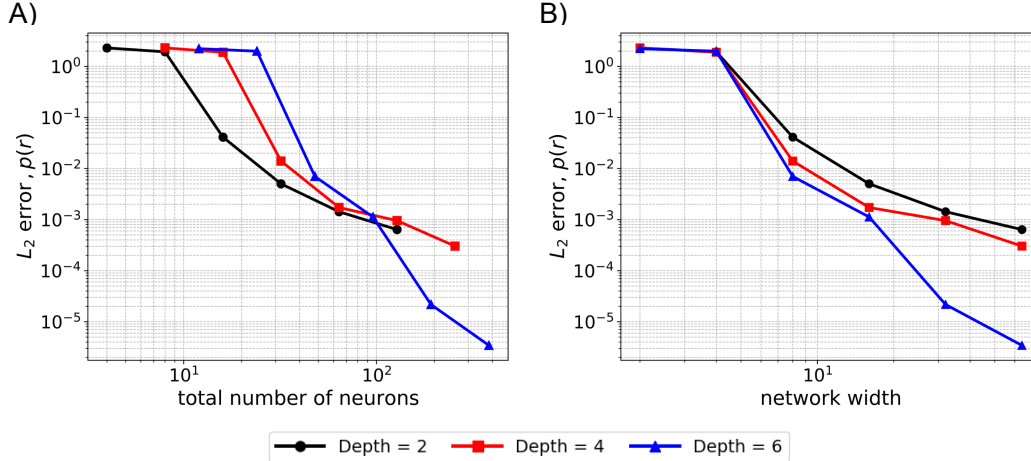


Figure 6. Gas flow through concentric cylinders. Convergence of the DeepLS approximation with increasing network capacity, characterized by the number of hidden layers L and the number of neurons per layer m . (A) $L_2(\Omega)$ error between the neural approximation \hat{u}_θ and the reference solution u_{ref} as a function of the total number of neurons N_{tot} for three depths ($L = 2, 4, 6$). (B) $L_2(\Omega)$ error as a function of the network width m for multiple depths ($L = 2, 4, 6$).

under-parameterized regime in which the trial space is insufficiently expressive and optimization can be challenging, particularly for deep but narrow networks. Beyond a moderate capacity threshold, the error drops rapidly by several orders of magnitude, marking an *expressive* regime in which the solution is represented with high accuracy. Notably, depth influences both the rate and onset of this decay: deeper networks attain lower errors once sufficient capacity is available but offer limited advantage when the width is too small.

To further disentangle the roles of depth and width, **Fig. 6B** plots the error versus network width m for fixed depths. The monotonic error reduction with increasing m reflects systematic enrichment of the trial space. At larger widths, the deeper network ($L = 6$) achieves a steeper accuracy gain, indicating that the solution benefits from the *compositional expressivity* of depth once width-induced bottlenecks are removed.

Taken together, these observations indicate that increasing network capacity must be balanced against computational cost, and that performance comparisons should account for both approximation power and optimization effects.

5.2. Footing problem. Engineering and near-surface flow problems frequently involve accessible boundaries along which pressurized, sealed, and vented regions coexist, leading to spatially heterogeneous boundary conditions with abrupt transitions between prescribed-pressure and prescribed-flux segments. In standard numerical approaches, such as finite element methods, these boundary configurations can induce localized steep gradients, flux singularities near boundary junctions, and heightened sensitivity to mesh resolution, often necessitating the use of stabilization techniques [Murad and Loula, 1992; Preisig and Prévost, 2011]. To systematically examine the behavior of the proposed framework under this heterogeneous boundary conditions we study a footing-type benchmark defined on a rectangular porous domain. A schematic of the problem is

shown in **Fig. 7**, and the material parameters and geometric details used in the simulation are summarized in **Table 3**.

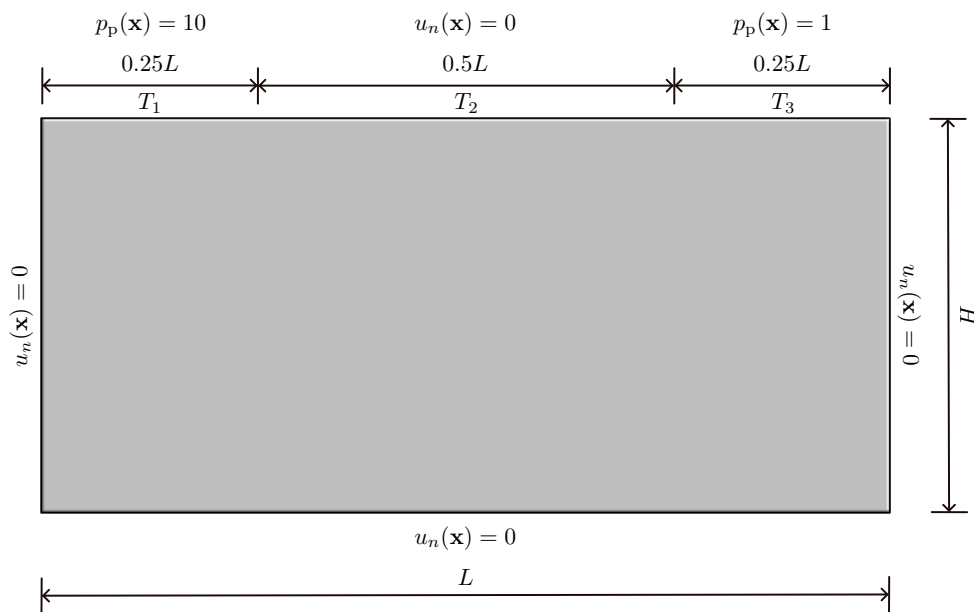


Figure 7. Footing problem. Schematic of the boundary value problem. The left, right, and bottom boundaries of the domain are impermeable and subject to a no-flux condition (i.e., the normal component of the seepage velocity vanishes, $\mathbf{u}(\mathbf{x}) \cdot \hat{\mathbf{n}}(\mathbf{x}) = 0$). The top boundary ($y = 5$) is partitioned into three contiguous segments: (i) T_1 ($0 \leq x \leq 2.5$), where a prescribed pressure $p_p(\mathbf{x}) = 10$ is applied; (ii) T_2 ($2.5 < x \leq 7.5$), where a no-flux condition $\mathbf{v}(\mathbf{x}) \cdot \hat{\mathbf{n}}(\mathbf{x}) = 0$ is enforced; and (iii) T_3 ($7.5 < x \leq 10$), where the boundary is vented (i.e., hydraulically connected to an external reservoir and maintained at the reference pressure $p_p(\mathbf{x}) = 1$).

Table 3. Footing problem. Material and geometry parameters.

| Parameter | Value |
|--|-----------------------|
| L | 10 |
| H | 5 |
| β | 1 |
| μ | 1 |
| $\phi(\mathbf{x}) \gamma \mathbf{b}(\mathbf{x})$ | $\mathbf{0} = [0, 0]$ |
| k_0 | 1 |

Figure 8 presents representative predicted fields obtained at a high collocation density, illustrating the spatial structure of the pressure field $p(\mathbf{x})$ and the corresponding distribution of the velocity magnitude $\|\mathbf{u}(\mathbf{x})\|$. **Figure 9** shows the error contours relative to the reference solution computed using a stabilized mixed finite element method, indicating that the approximation errors remain small throughout the domain. Finally, **Fig. 10** demonstrates that increasing the collocation

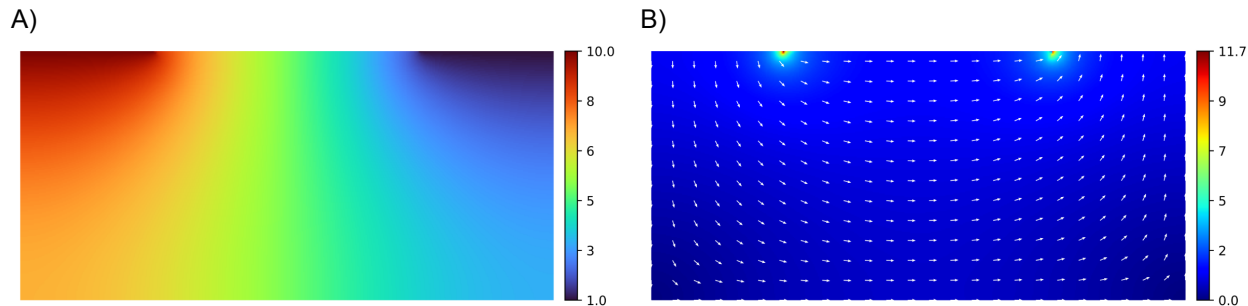


Figure 8. Footing problem. This figure illustrates DeepLS predictions computed using a collocation density of 12,000 points: (A) the pressure field, $p(\mathbf{x})$, and (B) the velocity-magnitude field, $\|\mathbf{u}(\mathbf{x})\|$.

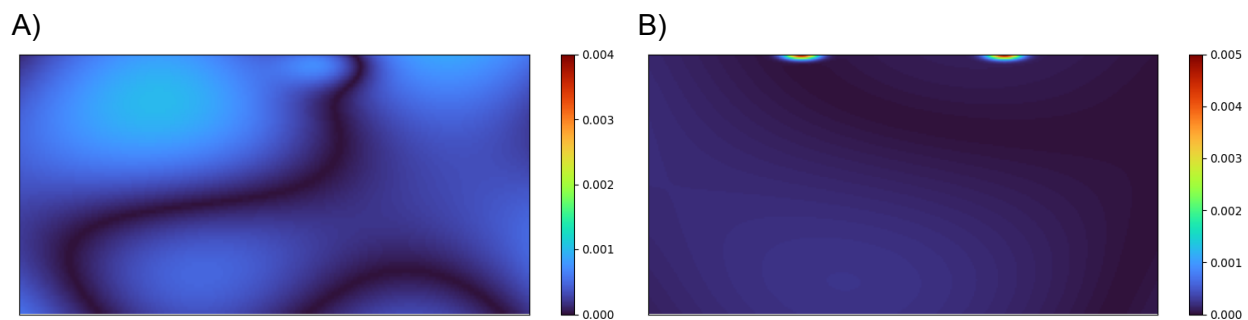


Figure 9. Footing problem. This figure illustrates absolute error between the DeepLS predictions and the corresponding finite element (FEM) solutions. The DeepLS results are obtained using a collocation point density of 12,000 points. The FEM reference solutions are computed using the stabilized formulation studied in Masud and Hughes [2002] and Nakshatrala et al. [2006]. The results indicate that the DeepLS predictions are in good agreement with the finite element solutions.

density systematically improves training behavior: the total loss exhibits smoother decay and converges to a lower terminal value, consistent with stronger enforcement of the governing equations and boundary conditions. These results were obtained using a neural network with six hidden layers and 64 neurons per layer, trained with the ReLU activation function; the total training time on an NVIDIA T4 GPU was 7.48 minutes.

5.3. Flow through a layered porous medium. This benchmark problem tests solver performance under sharp coefficient discontinuities, the key numerical challenge in modeling stratified porous media. Specifically, the problem examines whether the formulation (i) correctly redistributes flow across high- and low-permeability layers under identical boundary conditions, (ii) resolves interface-localized gradients without spurious oscillations, and (iii) maintains pressure continuity and physically consistent normal flux transfer as permeability contrasts increase.

To illustrate this, we consider gas flow in a rectangular porous domain of length $L = 5$ and height $H = 4$, divided into five horizontal layers with piecewise-constant permeabilities, as shown in **Fig. 11**. A pressure difference is imposed between the left and right boundaries, while the top and bottom boundaries are impermeable, i.e., $\mathbf{u}(\mathbf{x}) \cdot \hat{\mathbf{n}}(\mathbf{x}) = 0$, material parameters and geometry

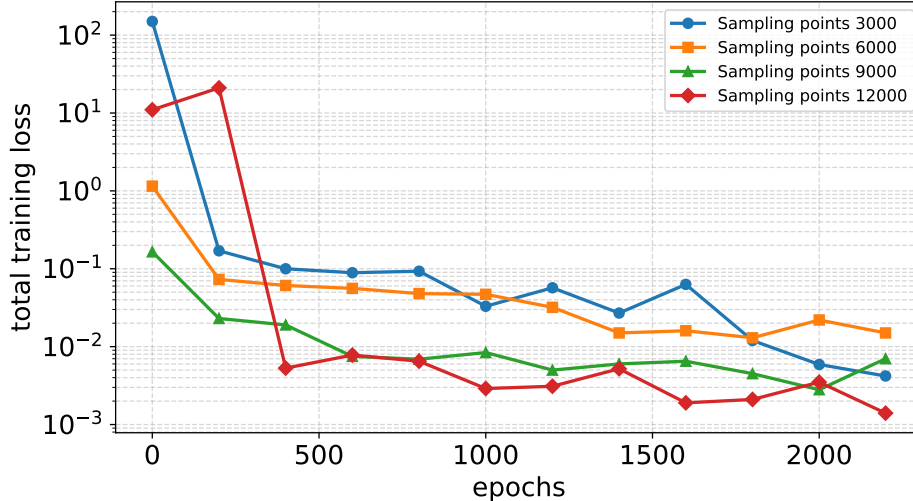


Figure 10. Footing problem. This figure shows the evolution of the total training loss over epochs for different collocation densities. Each curve corresponds to an independent optimization run initialized with 3,000, 6,000, 9,000, and 12,000 collocation points. Increasing the collocation density yields faster convergence and a lower terminal loss, indicating more stable optimization and improved solution fidelity (i.e., the learned model exhibits reduced residuals with respect to the governing equations).

details used in the simulation are summarized in Table 4. Because the layers are aligned with the coordinate axes, permeability changes occur only across horizontal interfaces, leading to layer-dependent pressure gradients and flow distribution.

Table 4. Flow through a layered porous medium. Material and geometry parameters.

| Parameter | Value |
|--|-----------------------|
| L | 5 |
| H | 4 |
| β | 1 |
| μ | 1 |
| $\phi(\mathbf{x}) \gamma \mathbf{b}(\mathbf{x})$ | $\mathbf{0} = [0, 0]$ |
| p^{left} | 10 |
| p^{right} | 1 |

Figure 12 demonstrates that the predicted pressure field remains smooth and continuous across material interfaces while the velocity field exhibits pronounced layer-wise contrasts that reflect permeability variations. **Figure 13** shows a horizontal velocity profile u_x evaluated at ($x = 2.5$), revealing a distinct step-like structure that directly mirrors the underlying stratification. The sharp yet stable transitions between layers confirm that the method captures velocity profile without spurious oscillations, even in the presence of strong variations in permeability. These results were obtained using a neural network with eight hidden layers and 128 neurons per layer, trained with the ReLU activation function; the total training time on an NVIDIA T4 GPU was 8.38 minutes.

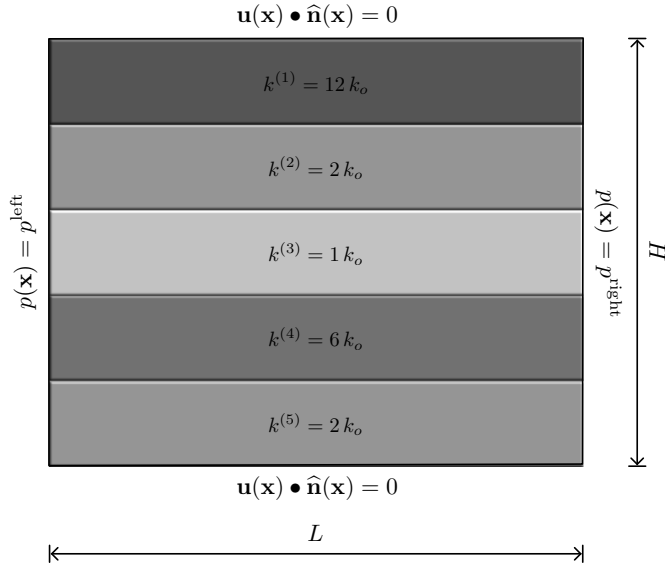


Figure 11. Flow through a layered porous medium. This figure illustrates gas flow in layered media. A rectangular domain ($L = 5, H = 4$) is composed of five horizontal layers, each with a distinct (piecewise constant) intrinsic permeability. A left-to-right pressure drop is enforced by prescribing ($p^{\text{left}} = 10$) on the inlet boundary and ($p^{\text{right}} = 1$) on the outlet boundary, while the top and bottom boundaries are impermeable ($(\mathbf{u}(\mathbf{x}) \cdot \hat{\mathbf{n}}(\mathbf{x}) = 0)$). This configuration is used to assess how pressure-dependent Klinkenberg slip modifies the pressure and velocity fields across permeability contrasts.

5.4. Gas flow through concentric spheres. The motivation for studying this configuration is twofold. *Engineering-wise*, concentric spherical domains are common in gas-transport applications involving layered or encapsulated media, such as subsurface migration around cavities and pressure-driven flow through spherical pellets, membranes, and porous shells [Pruess et al., 2012; Tsang and Neretnieks, 1998]. *Numerically*, the problem provides a stringent benchmark for evaluating the robustness of the proposed DeepLS framework in capturing three-dimensional radial symmetry and handling curved geometries.

To increase the numerical challenge, only a half-domain is modeled and symmetry boundary conditions are imposed, leading to a zero-velocity constraint on the symmetry plane (with quarter-domain reduction also possible). This results in mixed boundary conditions. In conventional finite element methods, enforcing such conditions—especially no-penetration constraints on nonconforming planar boundaries—typically requires Nitsche-type weak enforcement [Joodat et al., 2018]. By contrast, DeepLS embeds these constraints directly into the loss functional, enabling accurate pressure and flux predictions without additional stabilization, which will be demonstrated using this numerical example.

We consider gas flow in a concentric spherical domain bounded by an inner sphere of radius r_i and an outer sphere of radius r_o . The inner and outer spherical surfaces are prescribed with pressures p_i and p_o while a no-flux boundary condition is imposed on the planar surface $z = r_o$ as illustrated in **Fig. 14**. Material properties and geometric parameters used in the simulations are summarized in Table 2.

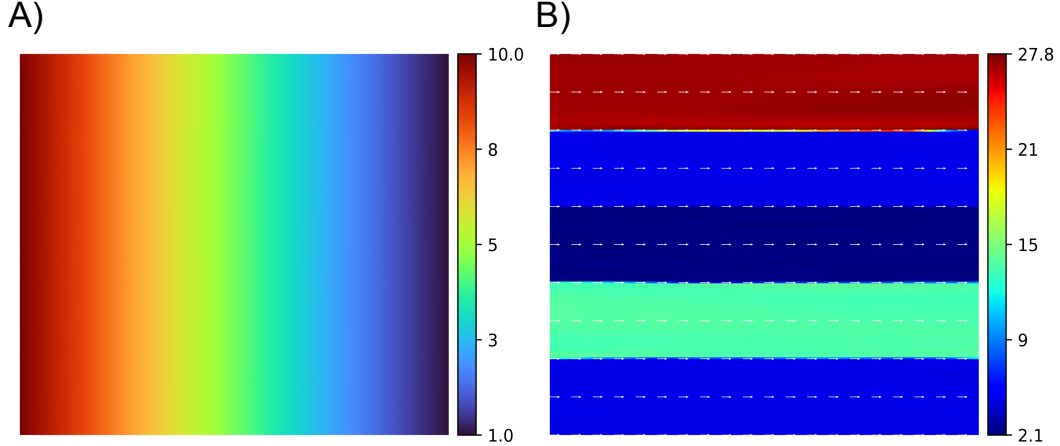


Figure 12. Flow through a layered porous medium. This figure showcases the DeepLS results for Klinkenberg gas flow in a layered medium, highlighting interface-resolving behavior. (A) Predicted pressure field exhibits a smooth, essentially one-dimensional left-to-right drop, remaining continuous across material interfaces as required by the governing flow model. (B) Velocity field (magnitude contours with direction vectors) shows strong layer-to-layer contrasts, with flow accelerating in more conductive layers and decelerating in less conductive layers; the vectors remain predominantly aligned with the imposed pressure gradient.

This boundary-value problem admits an analytical solution of the following form:

$$p(r) = \beta p_{\text{atm}} W\left(\frac{1}{\beta p_{\text{atm}}} \exp\left(\frac{\mathcal{P}(r)}{\beta p_{\text{atm}}}\right)\right) \quad (5.5)$$

$$u_r(r) = \frac{k_0}{\mu} \left((p_i - p_o) + \beta p_{\text{atm}} \ln\left(\frac{p_i}{p_o}\right) \right) \frac{r_i r_o}{r_0 - r_i} \frac{1}{r^2} \quad (5.6)$$

where $\mathcal{P}(r)$ is given by:

$$\mathcal{P}(r) = \mathcal{P}_o + (\mathcal{P}_i - \mathcal{P}_o) \frac{r_i r_o}{r_o - r_i} \left(\frac{1}{r} - \frac{1}{r_o} \right) \quad (5.7)$$

Figure 15 shows that the DeepLS model produces a radially structured solution on the concentric-sphere geometry: the pressure varies smoothly between the prescribed inner and outer values, while the velocity magnitude is largest near the inner sphere and decreases with radius, consistent with geometric spreading in spherical flow. **Figure 16** confirms this behavior through comparison with the closed-form solution, showing near-perfect agreement between the predicted and analytical radial pressure $p(r)$ and velocity $u_r(r)$ profiles. This close agreement demonstrates accurate recovery of both the pressure field and the associated radial flux.

Notably, for this boundary value problem, the proposed DeepLS framework outperforms standard finite element workflows in terms of formulation and enforcement: it achieves this level of accuracy without mesh generation or auxiliary weak-enforcement techniques (e.g., Nitsche-type methods [Joodat et al., 2018; Schillinger et al., 2016]) commonly required in conventional approaches. **Figure 17** presents the $L_2(\Omega)$ errors as the network width increases for several fixed depths. Errors in both pressure and velocity decrease with increasing width before saturating, while, for a fixed width, deeper networks consistently yield lower errors, highlighting the accuracy gains enabled by increased network depth. These results were obtained using a neural network with

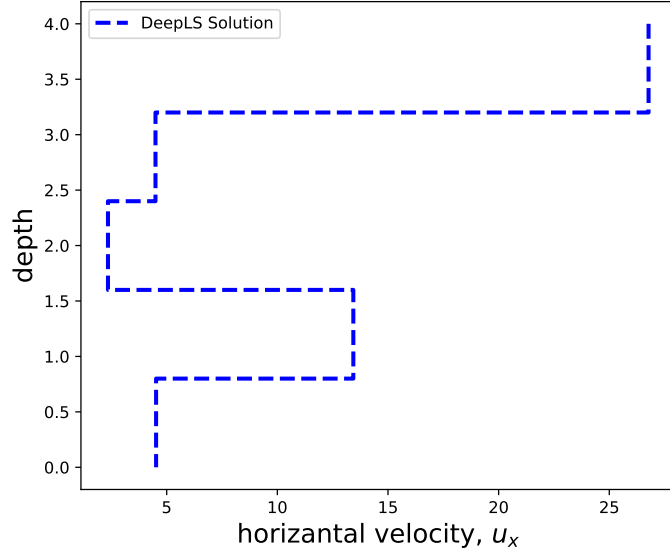


Figure 13. Flow through a layered porous medium. This figure illustrates the depthwise profile of the velocity magnitude obtained from the DeepLS solution. The results exhibit a distinct step-like structure that closely reflects the underlying layered architecture, indicating that the method accurately captures sharp interfacial variations in flux. Such features would typically require specialized treatments—such as Discontinuous Galerkin formulations in finite element methods—to properly resolve flux discontinuities across material interfaces [Joshaghani et al., 2019].

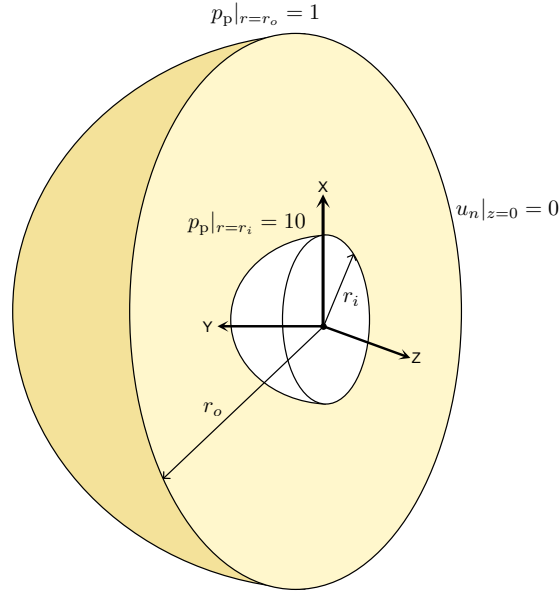


Figure 14. Gas flow through concentric spheres. This figure illustrates the computational geometry and boundary conditions. The domain is defined by an inner sphere of radius r_i and an outer sphere of radius r_o . Prescribed pressure boundary conditions are imposed on the inner and outer spherical surfaces, while a no-normal-flux condition is enforced on the planar surface defined by $z = 0$.

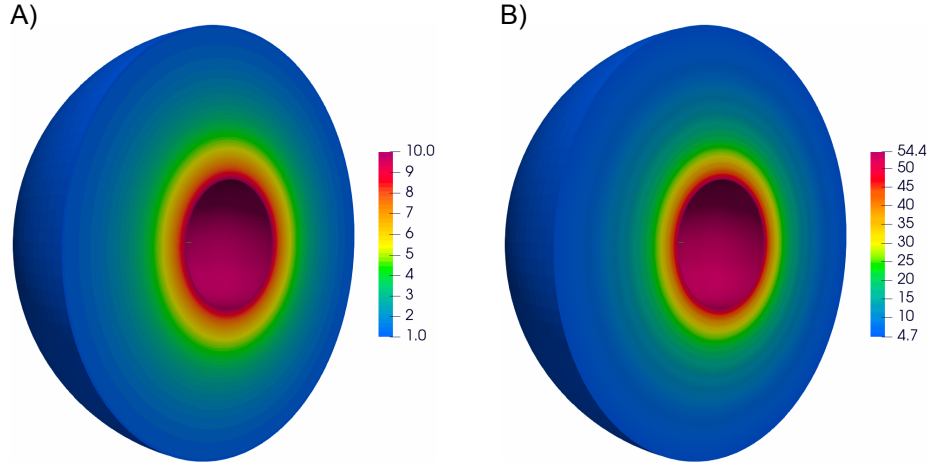


Figure 15. Gas flow through concentric spheres. (A) shows the predicted pressure field within the spherical shell, illustrating the smooth pressure decay from the inner to the outer spherical boundary and accurate enforcement of the prescribed pressure conditions. (B) shows the magnitude of the velocity, highlighting the radially varying flow intensity and the expected increase in velocity near the inner sphere. The results demonstrate the ability of the DeepLS framework to resolve both pressure and velocity fields in a fully three-dimensional curved geometry without mesh-based discretization.

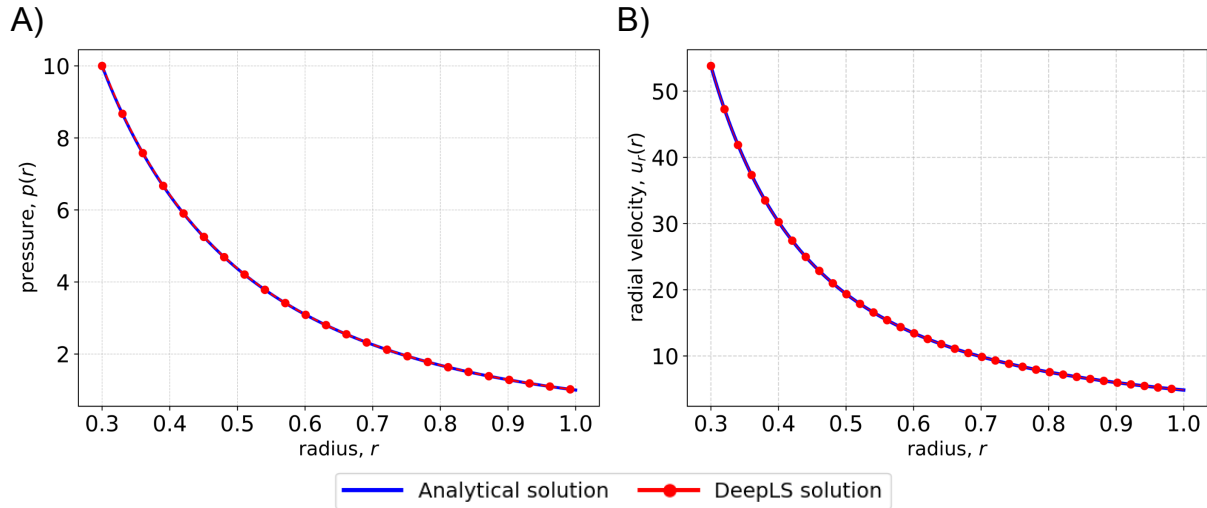


Figure 16. Gas flow through concentric spheres. This figure illustrates comparison between analytical solution with the DeepLS prediction. (A) Radial pressure $p(r)$ and (B) radial Darcy velocity $u_r(r)$. The DeepLS prediction overlap the analytical solution profiles confirming accurate recovery of both fields.

eight hidden layers and 128 neurons per layer, trained with the ReLU activation function; the total training time on an NVIDIA T4 GPU was 8.26 minutes.

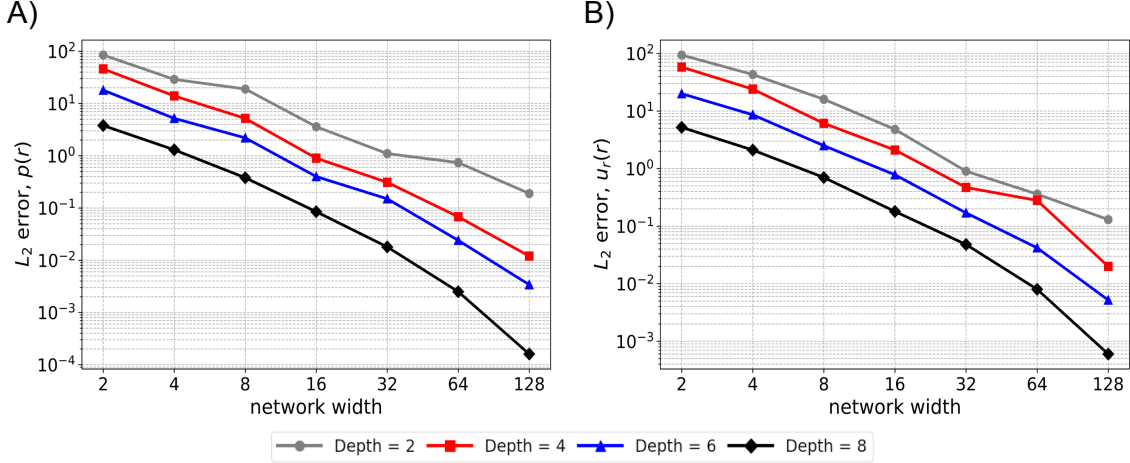


Figure 17. Gas flow through concentric spheres. This figure shows $L_2(\Omega)$ errors of the DeepLS predictions as the network width is increased for several fixed depths. (A) $L_2(\Omega)$ error in the predicted pressure field, $\|p - p_{\text{ref}}\|_{L_2(\Omega)}$. (B) $L_2(\Omega)$ error in the predicted velocity field, $\|\mathbf{u} - \mathbf{u}_{\text{ref}}\|_{L_2(\Omega)}$. The reference fields p_{ref} and \mathbf{u}_{ref} correspond to the analytical solution. As network width increases, the $L_2(\Omega)$ errors in both pressure and velocity decrease and then level off, indicating a diminishing-returns regime once sufficient capacity is reached. For a fixed width, deeper networks consistently yield smaller errors, showing that depth improves approximation quality.

6. MECHANICS-BASED VERIFICATION

Recently, [Maduri and Nakshatrala \[2025\]](#) established a reciprocal relation for a nonlinear porous-media flow model with pressure-dependent viscosity. Building on this work, we employ the Hopf–Cole transformation to recover reciprocity for the Klinkenberg model, yielding a consistent framework for evaluating reciprocity residuals across different network architectures. Within this framework, we use a Betti-type reciprocity relation as a mechanics-based *a posteriori* error indicator and examine its sensitivity to the depth and width of the neural network architecture.

Betti’s reciprocal theorem for the Klinkenberg model may thus be stated as follows. Let $(p^{(1)}(\mathbf{x}), \mathbf{u}^{(1)}(\mathbf{x}))$ and $(p^{(2)}(\mathbf{x}), \mathbf{u}^{(2)}(\mathbf{x}))$ denote the solutions associated with two distinct sets of boundary data, $(p_p^{(1)}(\mathbf{x}), u_n^{(1)}(\mathbf{x}))$ and $(p_p^{(2)}(\mathbf{x}), u_n^{(2)}(\mathbf{x}))$, respectively. These fields satisfy the following identity:

$$\begin{aligned}
& \int_{\Gamma_u} u_n^{(2)}(\mathbf{x}) \left(p^{(1)}(\mathbf{x}) + \beta p_{\text{atm}} \ln [p^{(1)}(\mathbf{x})] \right) d\Gamma \\
& - \int_{\Gamma_p} \left(p_p^{(2)}(\mathbf{x}) + \beta p_{\text{atm}} \ln [p_p^{(2)}(\mathbf{x})] \right) \mathbf{u}^{(1)}(\mathbf{x}) \bullet \hat{\mathbf{n}}(\mathbf{x}) d\Gamma \\
& = \int_{\Gamma_u} u_n^{(1)}(\mathbf{x}) \left(p^{(2)}(\mathbf{x}) + \beta p_{\text{atm}} \ln [p^{(2)}(\mathbf{x})] \right) d\Gamma \\
& - \int_{\Gamma_p} \left(p_p^{(1)}(\mathbf{x}) + \beta p_{\text{atm}} \ln [p_p^{(1)}(\mathbf{x})] \right) \mathbf{u}^{(2)}(\mathbf{x}) \bullet \hat{\mathbf{n}}(\mathbf{x}) d\Gamma \quad (6.1)
\end{aligned}$$

6.1. Application to the footing problem. We apply this identity to the footing problem described in Subsection 5.2. This problem is particularly well suited for the present study because it does not admit a closed-form analytical solution, thereby providing a meaningful setting for mechanics-based verification. For both solution states, the normal component of the velocity vanishes on Γ_u :

$$u_n^{(1)}(\mathbf{x}) = 0 \quad \text{and} \quad u_n^{(2)}(\mathbf{x}) = 0 \quad \forall \mathbf{x} \in \Gamma_u \quad (6.2)$$

As a consequence, the integrals over Γ_u in Eq. (6.1) vanish identically, and the reciprocal relation reduces to

$$\begin{aligned} \mathcal{R}_B := & \int_{\Gamma_p} \left(p_p^{(2)}(\mathbf{x}) + \beta p_{\text{atm}} \ln [p_p^{(2)}(\mathbf{x})] \right) \mathbf{u}^{(1)}(\mathbf{x}) \bullet \hat{\mathbf{n}}(\mathbf{x}) \, d\Gamma \\ & - \int_{\Gamma_p} \left(p_p^{(1)}(\mathbf{x}) + \beta p_{\text{atm}} \ln [p_p^{(1)}(\mathbf{x})] \right) \mathbf{u}^{(2)}(\mathbf{x}) \bullet \hat{\mathbf{n}}(\mathbf{x}) \, d\Gamma = 0 \end{aligned} \quad (6.3)$$

Given that for the exact solution fields, the residual satisfies $\mathcal{R}_B = 0$, the magnitude $|\mathcal{R}_B|$ provides an *a posteriori* verification metric for assessing numerical accuracy. To enable meaningful comparisons across different neural network architectures, we define the normalized reciprocity error as follows:

$$\eta_B := \frac{|\mathcal{I}_{12} - \mathcal{I}_{21}|}{|\mathcal{I}_{12}| + |\mathcal{I}_{21}|} = \frac{|\mathcal{R}_B|}{|\mathcal{I}_{12}| + |\mathcal{I}_{21}|} \quad (6.4)$$

where

$$\mathcal{I}_{12} := \int_{\Gamma_p} \left(p_p^{(2)}(\mathbf{x}) + \beta p_{\text{atm}} \ln [p_p^{(2)}(\mathbf{x})] \right) \mathbf{u}^{(1)}(\mathbf{x}) \bullet \hat{\mathbf{n}}(\mathbf{x}) \, d\Gamma \quad (6.5)$$

$$\mathcal{I}_{21} := \int_{\Gamma_p} \left(p_p^{(1)}(\mathbf{x}) + \beta p_{\text{atm}} \ln [p_p^{(1)}(\mathbf{x})] \right) \mathbf{u}^{(2)}(\mathbf{x}) \bullet \hat{\mathbf{n}}(\mathbf{x}) \, d\Gamma \quad (6.6)$$

The normalized quantity η_B is evaluated for networks of varying width and depth and reported as a function of architectural complexity, thereby quantifying the influence of representational capacity on the degree to which the reciprocity condition is satisfied.

Figure 18 shows that the normalized reciprocity error decreases with increasing network width for all considered depths, but plateaus beyond a moderate width, indicating diminishing returns from further widening. In contrast, increasing network depth leads to consistently lower reciprocity errors at comparable widths. These observations suggest that, for a fixed parameter budget, increasing depth is a more efficient strategy than increasing width for improving satisfaction of the reciprocity condition.

7. CLOSURE

This work developed a stable and mathematically well-posed framework that integrates deep learning with continuum modeling to simulate gas flow through porous media in regimes where gas slippage invalidates classical Darcy formulations due to the pressure dependence of the apparent gas permeability. By extending the Hopf–Cole transformation to the Klinkenberg permeability model, the nonlinear governing equations are recast into an equivalent linear Darcy-type system, yielding improved analytical tractability and numerical conditioning. The resulting formulation admits a least-squares representation with a symmetric and positive-definite operator, enabling robust and

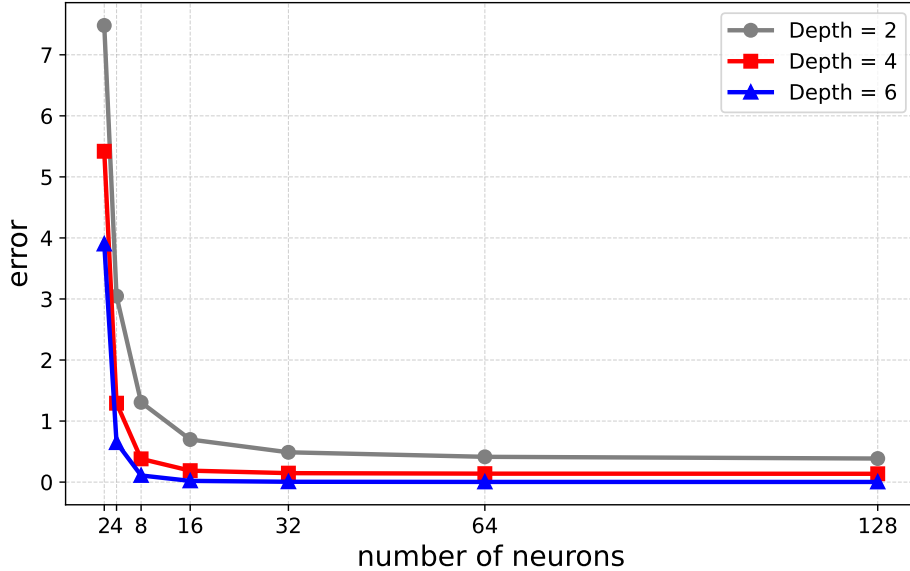


Figure 18. Betti relation. This figure shows normalized reciprocity error against the number of neurons per hidden layer for multiple network depths. All simulations are performed for fixed interior and boundary point sets, ensuring that variations in the reciprocity error are attributable to changes in network representational capacity. Increasing width generally reduces reciprocity violation, while deeper architectures attain smaller errors at comparable widths.

stable solution strategies. A mixed pressure–velocity formulation implemented through a shared-trunk neural architecture ensures physically consistent prediction of both fields, while a rigorous convergence analysis establishes the theoretical soundness of the proposed DeepLS-based approach. Overall, the integration of transformed continuum models with physics-informed learning provides a computationally efficient and interpretable alternative to pore-scale simulation for non-Darcy gas transport in tight and low-pressure formations.

Some of the main contributions of this work are summarized as follows:

- (C1) **Accuracy:** Numerical solutions obtained with the framework are in close agreement with corresponding finite element solutions, with convergence behavior demonstrated on canonical benchmark problems.
- (C2) **Mathematical analysis:** A rigorous convergence analysis is developed, establishing the stability and reliability of the method.
- (C3) **Computational efficiency:** Computational cost is quantified through time-to-solution measurements, highlighting the efficiency of the approach.
- (C4) **Enhanced modeling capability:** The framework accurately resolves velocity fields in porous media with strong heterogeneity, including layered domains with highly disparate permeabilities.

Beyond the specific Klinkenberg model considered here, the methodology provides a general pathway for combining analytical transformations, mixed formulations, and least-squares learning to address nonlinear and multiscale transport problems, with clear potential for extension to heterogeneous, multiphysics, and coupled flow systems. Future research directions include:

- (i) extending the framework to multiphase flow systems, where additional nonlinearities such as capillarity and phase interactions further complicate the modeling process;
- (ii) integrating uncertainty quantification techniques within the neural network architecture to enable more informed decision-making in reservoir engineering and risk assessment; and
- (iii) investigating performance on high-performance computing platforms to facilitate large-scale, real-time simulations in industrial settings.

Appendix A. The real-valued Lambert–W function

The Lambert– W function, also known as the product logarithm, is defined as the inverse of the real-valued mapping

$$w \mapsto we^w \tag{A.1}$$

For a real argument x , the Lambert– W function is defined implicitly by the relation

$$W(x)e^{W(x)} = x \tag{A.2}$$

Real-valued branches of the Lambert– W function exist only for $x \geq -1/e$. On this domain, the function admits one or two real branches depending on the value of x . The principal branch, denoted by $W_0(x)$, is defined for $x \geq -1/e$ and satisfies $W_0(x) \geq -1$. The secondary branch, denoted by $W_{-1}(x)$, is defined on the interval $-1/e \leq x < 0$ and satisfies $W_{-1}(x) \leq -1$. These two branches meet at the branch point $x = -1/e$, where

$$W_0(-1/e) = W_{-1}(-1/e) = -1 \tag{A.3}$$

Figure 19 illustrates the two real branches of the Lambert– W function.

The Lambert– W function is particularly useful for solving real transcendental equations in which the unknown variable appears both algebraically and exponentially. For example, the equation

$$xe^x = a \tag{A.4}$$

admits the explicit solution

$$x = W(a) \tag{A.5}$$

provided that $a \geq -1/e$. This property is exploited in the present work through the inverse Hopf–Cole transformation (see §3.4). For a comprehensive discussion of the real-valued Lambert– W function and its applications, see [Corless et al. \[1996\]](#) and [Olver et al. \[2010\]](#).

DATA AND CODE AVAILABILITY STATEMENT

All data generated in this study are synthetic and reproducible using the publicly available source code, which will be released upon publication at <https://github.com/CAMLKBN/DeepLSCodes>. Additional supporting data are available from the corresponding author upon reasonable request.

Funding Declaration. The authors acknowledge the support from the Environmental Molecular Sciences Laboratory (EMSL), a DOE Office of Science User Facility sponsored by the Biological and Environmental Research program under contract no: DE-AC05-76RL01830 (Large-Scale Research User Project No: 60720, Award DOI: [10.46936/1ser.proj.2023.60720/60008914](https://doi.org/10.46936/1ser.proj.2023.60720/60008914)). The views and opinions of authors expressed herein do not necessarily state or reflect those of the United States Government or any agency thereof.

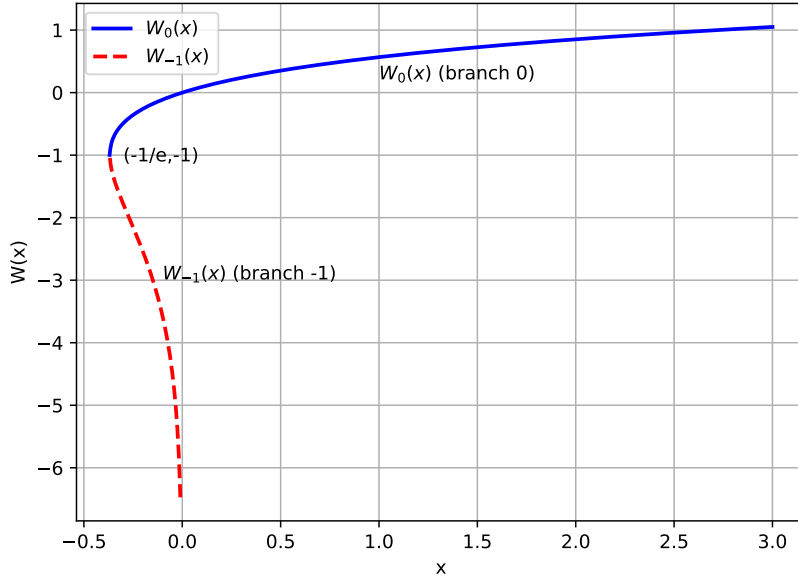


Figure 19. Graph of the Lambert– W function showing both branches. In this work, only the principal branch $W_0(x)$ (branch 0) is relevant, since the pressure field to which the Lambert– W transformation is applied is strictly positive. For $x > 0$, the mapping is bijective. For $x \in [-e^{-1}, 0)$, the function admits two real branches, $W_0(x)$ and $W_{-1}(x)$, and is therefore not single-valued. Of course, the function is undefined for $x < -e^{-1}$.

Declaration of Competing Interests. The authors declare that they have no known competing financial interests or personal relationships that could have appeared to influence the work reported in this paper.

References

- R. A. Adams and J. J. F. Fournier. *Sobolev Spaces*, volume 140 of *Pure and Applied Mathematics*. Elsevier, Amsterdam, 2nd edition, 2003.
- J. Bear. *Dynamics of Fluids in Porous Media*. Dover Publications, Inc., New York, 2013.
- J. Bear and A. H.-D. Cheng. *Modeling Groundwater Flow and Contaminant Transport*. Springer, Dordrecht, 2010.
- M. Bernkopf and J. M. Melenk. Optimal convergence rates in L^2 for a first order system least squares finite element method-part II: Inhomogeneous Robin boundary conditions. *Computers & Mathematics with Applications*, 173:1–18, 2024. DOI: [10.1016/j.camwa.2024.07.035](https://doi.org/10.1016/j.camwa.2024.07.035).
- F. M. Bersetche and J. P. Borthagaray. A deep first-order system least-squares method for solving elliptic PDEs. *Computers & Mathematics with Applications*, 129:136–150, 2023. DOI: [10.1016/j.camwa.2022.11.014](https://doi.org/10.1016/j.camwa.2022.11.014).
- A. Beskok and G. E. Karniadakis. A report on the lattice Boltzmann method for rarefied gas flows. *Journal of Thermophysics and Heat Transfer*, 13(3):319–329, 1999. DOI: [10.2514/2.648](https://doi.org/10.2514/2.648).
- M. J. Blunt. Multiphase Flow in Porous Media. *Annual Review of Fluid Mechanics*, 49:253–272, 2017. DOI: [10.1146/annurev-fluid-010816-060259](https://doi.org/10.1146/annurev-fluid-010816-060259).
- D. Boffi, F. Brezzi, and M. Fortin. *Mixed Finite Element Methods and Applications*. Springer, Berlin, 2013.

- S. C. Brenner and L. R. Scott. *The Mathematical Theory of Finite Element Methods*. Springer, New York, 2008.
- H. Brezis. *Functional Analysis, Sobolev Spaces and Partial Differential Equations*, volume 2. Springer, New York, 2011.
- F. Brezzi and M. Fortin. *Mixed and Hybrid Finite Element Methods*. Springer, New York, 1991.
- E. Burman and R. Puppi. Two mixed finite element formulations for the weak imposition of the Neumann boundary conditions for the Darcy flow. *Journal of Numerical Mathematics*, 30(2): 141–162, 2022. DOI: [10.1515/jnma-2021-0042](https://doi.org/10.1515/jnma-2021-0042).
- Z. Cai, J. Chen, M. Liu, and X. Liu. Deep least-squares methods: An unsupervised learning-based numerical method for solving elliptic PDEs. *Journal of Computational Physics*, 420:109707, 2020. DOI: [10.1016/j.jcp.2020.109707](https://doi.org/10.1016/j.jcp.2020.109707).
- R. Caruana. Multitask learning. *Machine Learning*, 28(1):41–75, 1997. DOI: [10.1023/A:1007379606734](https://doi.org/10.1023/A:1007379606734).
- F. Civan. *Reservoir Formation Damage: Fundamentals, Modeling, Assessment, and Mitigation*. Elsevier, Oxford, 2nd edition, 2010.
- J. D. Cole. On a quasi-linear parabolic equation occurring in aerodynamics. *Quarterly of Applied Mathematics*, 9:225–236, 1951. DOI: [10.1090/qam/42889](https://doi.org/10.1090/qam/42889).
- R. M. Corless, G. H. Gonnet, D. E. Hare, D. J. Jeffrey, and D. E. Knuth. On the Lambert W function. *Advances in Computational Mathematics*, 5:329–359, 1996. DOI: [10.1007/BF02124750](https://doi.org/10.1007/BF02124750).
- F. A. L. Dullien. *Porous Media: Fluid Transport and Pore Structure*. Academic Press, San Diego, 2nd edition, 1992.
- W. E and B. Yu. The deep Ritz method: A deep learning-based numerical algorithm for solving variational problems. *Communications in Mathematics and Statistics*, 6(1):1–12, 2018. DOI: [10.1007/s40304-018-0127-z](https://doi.org/10.1007/s40304-018-0127-z).
- L. C. Evans. *Partial Differential Equations*. American Mathematical Society, Providence, 1998.
- F. P. Florence, J. A. Rushing, K. E. Newsham, and T. A. Blasingame. Improved permeability predictions in tight gas sands using pressure-dependent permeability and Klinkenberg-corrected gas permeability. In *SPE Annual Technical Conference and Exhibition*. Society of Petroleum Engineers, 2007. DOI: [10.2118/107954-MS](https://doi.org/10.2118/107954-MS).
- R. A. Freeze and J. A. Cherry. *Groundwater*. Prentice-Hall, Englewood Cliffs, New Jersey, 1979.
- G. F. Froment, K. B. Bischoff, and J. De Wilde. *Chemical Reactor Analysis and Design*. John Wiley & Sons, Hoboken, 3rd edition, 2010.
- V. Girault and P.-A. Raviart. *Finite Element Methods for Navier–Stokes Equations: Theory and Algorithms*, volume 5 of *Springer Series in Computational Mathematics*. Springer-Verlag, Berlin, 1986.
- I. Gühring, G. Kutyniok, and P. Petersen. Error bounds for approximations with deep ReLU neural networks in $W^{s,p}$ norms. *Analysis and Applications*, 18(5):803–859, 2020. DOI: [10.1142/S0219530519410021](https://doi.org/10.1142/S0219530519410021).
- J. Heid, W. W. Owens, and R. L. Reed. Studies on gas flow through reservoir rocks. *Journal of Petroleum Technology*, 2(9):265–272, 1950. DOI: [10.2118/950265-G](https://doi.org/10.2118/950265-G).
- C. K. Ho and S. W. Webb, editors. *Gas Transport in Porous Media*, volume 20 of *Theory and Applications of Transport in Porous Media*. Springer, Dordrecht, Netherlands, 2006.
- E. Hopf. The partial differential equation $u_t + uu_x = \mu u_{xx}$. *Communications on Pure and Applied Mathematics*, 3:201–230, 1950. DOI: [10.1002/cpa.3160030302](https://doi.org/10.1002/cpa.3160030302).

- F. Javadpour. Nanopore gas flow in shale gas reservoirs. *Journal of Canadian Petroleum Technology*, 48(08):16–21, 2009. DOI: [10.2118/117494-PA](https://doi.org/10.2118/117494-PA).
- S. H. S. Joodat, K. B. Nakshatrala, and R. Ballarini. Modeling flow in porous media with double porosity/permeability: A stabilized mixed formulation, error analysis, and numerical solutions. *Computer Methods in Applied Mechanics and Engineering*, 337:632–676, 2018. DOI: [10.1016/j.cma.2018.04.004](https://doi.org/10.1016/j.cma.2018.04.004).
- M. S. Joshaghani, S. H. S. Joodat, and K. B. Nakshatrala. A stabilized mixed discontinuous Galerkin formulation for double porosity/permeability model. *Computer Methods in Applied Mechanics and Engineering*, 352:508–560, 2019. DOI: [10.1016/j.cma.2019.04.010](https://doi.org/10.1016/j.cma.2019.04.010).
- G. E. Karniadakis, I. G. Kevrekidis, L. Lu, P. Perdikaris, S. Wang, and L. Yang. Physics-informed machine learning. *Nature Reviews Physics*, 3:422–440, 2021. DOI: [10.1038/s42254-021-00314-5](https://doi.org/10.1038/s42254-021-00314-5).
- L. J. Klinkenberg. The permeability of porous media to liquids and gases. In *Drilling and Production Practice*, pages 200–213, New York, 1941. American Petroleum Institute.
- L. W. Lake, R. T. Johns, W. R. Rossen, and G. A. Pope. *Fundamentals of Enhanced Oil Recovery*. Society of Petroleum Engineers, Richardson, Texas, 2014.
- J.-J. Lions and E. Magenes. *Non-Homogeneous Boundary Value Problems and Applications*, volume I. Springer, Berlin, 1972.
- V. S. Maduri and K. B. Nakshatrala. Flow through porous media: A Hopf–Cole transformation approach for modeling pressure-dependent viscosity. *Journal of Applied Mechanics*, 92(11):111010, 2025. DOI: [10.1115/1.4069108](https://doi.org/10.1115/1.4069108).
- V. S. Maduri and K. B. Nakshatrala. An adaptive machine learning framework for fluid flow in dual-network porous media, 2026. Manuscript in preparation.
- M. Manav, R. Molinaro, S. Mishra, and L. De Lorenzis. Phase-field modeling of fracture with physics-informed deep learning. *Computer Methods in Applied Mechanics and Engineering*, 429:117104, 2024. DOI: [10.1016/j.cma.2024.117104](https://doi.org/10.1016/j.cma.2024.117104).
- A. Masud and T. J. R. Hughes. A stabilized mixed finite element method for Darcy flow. *Computer Methods in Applied Mechanics and Engineering*, 191(39-40):4341–4370, 2002. DOI: [10.1016/S0045-7825\(02\)00371-7](https://doi.org/10.1016/S0045-7825(02)00371-7).
- P. Monk. *Finite Element Methods for Maxwell’s Equations*. Numerical Mathematics and Scientific Computation. Oxford University Press, Oxford, 2003.
- M. A. Murad and A. F. D. Loula. Improved accuracy in finite element analysis of Biot’s consolidation problem. *Computer Methods in Applied Mechanics and Engineering*, 95(3):359–382, 1992. DOI: [10.1016/0045-7825\(92\)90193-N](https://doi.org/10.1016/0045-7825(92)90193-N).
- K. B. Nakshatrala, D. Z. Turner, K. D. Hjelmstad, and A. Masud. A stabilized mixed finite element method for Darcy flow based on a multiscale decomposition of the solution. *Computer Methods in Applied Mechanics and Engineering*, 195(33-36):4036–4049, 2006. DOI: [10.1016/j.cma.2005.07.009](https://doi.org/10.1016/j.cma.2005.07.009).
- F. W. J. Olver, D. W. Lozier, R. F. Boisvert, and C. W. Clark. *NIST Handbook of Mathematical Functions*. Cambridge University Press, Cambridge, 2010.
- M. Preisig and J. H. Prévost. Stabilization procedures in coupled poromechanics problems: A critical assessment. *International Journal for Numerical and Analytical Methods in Geomechanics*, 35(11):1207–1225, 2011. DOI: [10.1002/nag.951](https://doi.org/10.1002/nag.951).

- K. Pruess, C. Oldenburg, and G. Moridis. TOUGH2 User's Guide, Version 2.0. Technical Report LBNL-43134, Lawrence Berkeley National Laboratory, Berkeley, CA, 2012.
- M. Raissi, P. Perdikaris, and G. E. Karniadakis. Physics-informed neural networks: A deep learning framework for solving forward and inverse problems involving nonlinear partial differential equations. *Journal of Computational Physics*, 378:686–707, 2019. DOI: [10.1016/j.jcp.2018.10.045](https://doi.org/10.1016/j.jcp.2018.10.045).
- P.-A. Raviart and J.-M. Thomas. A mixed finite element method for second order elliptic problems. *Mathematical Aspects of Finite Element Methods*, 606:292–315, 1977. DOI: [10.1007/BFb0064470](https://doi.org/10.1007/BFb0064470).
- S. Ruder. An overview of multi-task learning in deep neural networks. *arXiv preprint arXiv:1706.05098*, 2017. URL <https://arxiv.org/abs/1706.05098>.
- T. D. Ryck, S. Lanthaler, and S. Mishra. On the approximation of functions by tanh neural networks. *Neural Networks*, 143:732–750, 2021. DOI: [10.1016/j.neunet.2021.08.015](https://doi.org/10.1016/j.neunet.2021.08.015).
- E. Samaniego, C. Anitescu, S. Goswami, V. M. Nguyen-Thanh, H. Guo, K. Hamdia, X. Zhuang, and T. Rabczuk. An energy approach to the solution of partial differential equations in computational mechanics via machine learning: Concepts, implementation and applications. *Computer Methods in Applied Mechanics and Engineering*, 362:112790, 2020. DOI: [10.1016/j.cma.2019.112790](https://doi.org/10.1016/j.cma.2019.112790).
- A. E. Scheidegger. *The Physics of Flow Through Porous Media*. University of Toronto Press, Toronto, 3rd edition, 1974.
- H. M. Schey. *Div, Grad, Curl, and All That*. W. W. Norton & Company, New York, 4 edition, 2005.
- D. Schillinger, I. Harari, M. C. Hsu, D. Kamensky, S. K. F. Stoter, Y. Yu, and Y. Zhao. The non-symmetric Nitsche method for the parameter-free imposition of weak boundary and coupling conditions in immersed finite elements. *Computer Methods in Applied Mechanics and Engineering*, 309:625–652, 2016. DOI: [10.1016/j.cma.2016.06.026](https://doi.org/10.1016/j.cma.2016.06.026).
- A. Shapiro, D. Dentcheva, and A. Ruszczyński. *Lectures on Stochastic Programming: Modeling and Theory*. Society for Industrial and Applied Mathematics (SIAM), Philadelphia, 2 edition, 2014.
- J. W. Siegel and J. Xu. Approximation rates for neural networks with general activation functions. *Neural Networks*, 128:313–321, 2020. DOI: [10.1016/j.neunet.2020.05.019](https://doi.org/10.1016/j.neunet.2020.05.019).
- C. F. Tsang and I. Neretnieks. Flow channeling in heterogeneous fractured rocks. *Reviews of Geophysics*, 36(2):275–298, 1998. DOI: [10.1029/97RG03319](https://doi.org/10.1029/97RG03319).
- P. Vadasz. Analytical solution to nonlinear thermal diffusion: Kirchhoff versus Cole-Hopf transformations. *Journal of Heat Transfer*, 132(12):121302–1–121302–6, 2010. DOI: [10.1115/1.4002325](https://doi.org/10.1115/1.4002325).
- A. W. van der Vaart and J. A. Wellner. *Weak Convergence and Empirical Processes: With Applications to Statistics*. Springer, New York, 1996.
- S. Whitaker. Flow in porous media. In N. P. Cheremisinoff, editor, *Handbook of Fluid Mechanics*, chapter 8, pages 8.1–8.37. McGraw-Hill, New York, 1986.
- S. Whitaker. *The Method of Volume Averaging*. Kluwer Academic Publishers, Dordrecht, 1999.
- Y.-S. Wu, K. Pruess, and P. Persoff. Gas flow in porous media with Klinkenberg effects. *Transport in porous Media*, 32(1):117–137, 1998. DOI: [10.1023/A:1006535211684](https://doi.org/10.1023/A:1006535211684).
- W. P. Ziemer. *Weakly Differentiable Functions: Sobolev Spaces and Functions of Bounded Variation*, volume 120 of *Graduate Texts in Mathematics*. Springer, New York, 2 edition, 2012.